

# Weak localization and magnetoresistance in two-chain ladder models

## Schwache Lokalisierung und Magnetowiderstand in Leitermodellen

Diploma Thesis of

**Michael Schneider**

At the Department of Physics  
Institut für Theorie  
der kondensierten Materie

Reviewer:	Prof. Dr. Alexander D. Mirlin
Second reviewer:	Prof. Dr. Alexander Shnirman
Advisors:	Dr. Sam T. Carr
	Dr. Igor V. Gornyi

Duration: 11. November 2010 – 11. November 2011



Als Ansichtsexemplar genehmigt von

.....

Karlsruhe, den 11.11.2011, Prof. Dr. Alexander D. Mirlin



# Erklärung zur Selbständigkeit

Hiermit erkläre ich, die vorliegende Arbeit selbstständig angefertigt und dabei nur die angegebenen Quellen und Hilfsmittel verwendet zu haben.

.....  
Karlsruhe, den 11.11.2011, Michael Schneider



# Acknowledgements

First of all I would like to thank Professor Alexander Mirlin for giving me the opportunity to write my diploma thesis in his group and for the insightful discussions about physics. I also would like to thank Professor Alexander Shnirman for accepting the second revision.

I am infinitely grateful to my advisors, Doctor Sam Carr and Doctor Igor Gornyi. Both of them helped me during the last year with guidance, lots of patience and professional knowledge. Without their help this work would not have been possible.

I also would like to thank my roommates Paul Baireuther, Ulf Briskot, Johannes Reuther, David Wendland, Philip Wollfarth and especially Tobias Sproll for fruitful discussions about my thesis and physics in general. Furthermore I would like to thank Thomas Neder and again Philip Wollfarth for proof-reading my thesis.

At last, I would like to thank my parents, Peter and Maria Schneider as well as my brother Martin and my sister Patricia. They supported me throughout my whole life and made me the person I am.



# Contents

<b>1. Introduction</b>	<b>1</b>
<b>2. Conductivity</b>	<b>3</b>
2.1. Disorder . . . . .	4
2.2. Quantum mechanical approach for the conductivity . . . . .	6
2.2.1. Drude Conductivity . . . . .	7
2.2.2. Diffuson . . . . .	7
2.2.3. Cooperon . . . . .	8
2.3. Weak Localization . . . . .	10
<b>3. 1D-systems</b>	<b>13</b>
3.1. Phenomenology of 1D-systems . . . . .	14
3.2. Methods in one dimension . . . . .	15
<b>4. Functional Bosonization</b>	<b>17</b>
4.1. General Derivation . . . . .	17
4.2. Diagrammatic Technique . . . . .	20
<b>5. Ladder Model</b>	<b>23</b>
5.1. Ladder without magnetic field . . . . .	23
5.2. Ladder with a magnetic field . . . . .	27
<b>6. Weak Localization in the 2-chain ladder</b>	<b>31</b>
6.1. Phenomenological approach . . . . .	33
6.2. Microscopic approach . . . . .	37
6.3. Comparison of the two approaches . . . . .	42
<b>7. Results</b>	<b>47</b>
<b>8. Conclusion</b>	<b>53</b>
<b>Deutsche Zusammenfassung</b>	<b>55</b>
<b>Bibliography</b>	<b>59</b>
<b>Appendix</b>	<b>63</b>
A. Calculation of the $\mathcal{W}$ -functions . . . . .	63
B. Matsubara sum for DC-current . . . . .	67
C. Full Greens function in the Functional Bosonization approach . . . . .	69



# 1. Introduction

One dimensional systems have been a very interesting field for a long time in condensed matter physics. The first theoretical approaches to treat these systems were performed in the fifties by Luttinger and Tomonaga [25, 35], who introduced the well known Luttinger Liquid, and by Mattis and Lieb [27]. Their work showed that one dimensional systems exhibit some very special properties which cannot be seen in higher dimensions. These results led to a strong interest of theoretical physicists in this field and nowadays a lot of good reviews are available [16, 18, 32].

Whereas the theory has existed since the 1950s, the experimentalists managed to catch up in the last decades. Nowadays lots of realizations of one dimensional systems exist like single-wall carbon nanotubes [7], cleaved-edge and V-groove semiconductor quantum wires [5, 23], quantum Hall-edges [21] or metallic nanowires [33]. Especially single-wall carbon nanotubes have received a lot of experimental attention. Different experiments show Luttinger Liquid-like behaviour of single-wall carbon nanotubes, as expected for strongly interacting electrons in one dimension.

One very interesting field in condensed matter physics is that of disordered systems. In 1958 Anderson stated that disorder can lead to localization of electrons [3], but it took more than 20 years to develop the theory of localization [1]. This theory shows that localization is very pronounced in one dimension. In fact, even arbitrarily weak disorder leads to full localization in a noninteracting one dimensional system [28].

Although the clean, interacting case (leading to a Luttinger Liquid) and the disordered, noninteracting case (leading to localization) are well understood, less is known about disordered, interacting 1D systems. As seen in higher dimensional systems, interactions give rise to a renormalization of impurities. This renormalization is again very special in one dimension, since even a single (renormalized) impurity leads to a decoupling of an infinite Luttinger Liquid into two independent parts at zero temperature [20]. However, the case of many impurities turned out to be a lot more difficult. The first attempts to treat the disordered Luttinger Liquid were done by Apel and Rice [4] and by Giamarchi and Schulz [17], but recently progress has been made in understanding the single-channel disordered Luttinger Liquid [6, 19].

An interesting effect caused by disorder is that of weak localization. Weak localization is a quantum mechanical interference effect between different paths performing a loop, resulting in quantum localization and in a decrease of conductivity. The strength of the localization is determined by coherence, which can be destroyed by e.g. inelastic scattering events.

This effect is called dephasing and introduces an according dephasing time  $\tau_\phi$ , which is connected to external parameters like interaction strength or temperature, but the way it is connected depends strongly on the dimensionality of the system.

The goal of this thesis is to calculate the weak localization correction to the conductivity of a spinless disordered 2-chain ladder. In this thesis we restrict ourselves to the case of strong dephasing  $\tau_\phi/\tau \ll 1$ . This assumption is valid for weakly disordered systems or for high enough temperatures. The weak localization correction is interesting for several reasons. First of all, the correction for a single chain has already been calculated [19, 37], so it is instructive to go one level further and to look at the 2-chain ladder. Also, the spinless 2-chain ladder is one of the simplest one dimensional systems which can exhibit magnetoresistance (induced by weak localization). This cannot be seen in the spinless single chain, since the magnetic field can be totally gauged out. However, the spinful single chain can exhibit magnetoresistance, the underlying mechanism is in this case the Zeeman splitting [36, 38].

Furthermore, single wall carbon nanotubes can be mapped onto the 2-chain ladder [24]. Experiments performed by Man and Morpurgo [26] show that carbon nanotubes exhibit magnetoresistance induced by weak localization. Although the magnetic field acts differently on nanotubes than on a 2-chain ladder, this thesis is the first step in deriving the weak localization correction of carbon nanotubes.

We will show in this thesis that the magnetic field *enhances* the weak localization in the 2-chain ladder. This effect is unexpected, since the magnetic field usually decreases weak localization. Furthermore, we will show that the magnetic field effectively decouples the two chains and we identify this effect as the cause for the enhancement of the weak localization. Eventually we will see that the expected behaviour of the weak localization correction can be observed for small magnetic fields for a specific set of parameters.

## Outline

This thesis is divided into two parts as follows:

Chapters 2-4 introduce the reader to the concepts used throughout the thesis. The content of these chapters is well-known and can also be found in the cited textbooks and papers in more detail.

In chapter 2 we give a brief introduction to the concepts of disordered solids and the quantum mechanical approach to the conductivity. Especially the effect of weak localization is presented in detail. Chapter 3 is devoted to interacting one dimensional systems. This chapter is very general and covers the phenomenology of one dimensional systems and sums up various methods which are used. The method we will use is called Functional Bosonization, this method is explained in detail in chapter 4.

The second part of the thesis (chapter 5-7) is devoted to the work which has been done during the thesis.

We introduce the underlying ladder model in chapter 5, especially the case of the ladder in a magnetic field is accounted in this chapter. The actual calculation of the weak localization correction is performed in chapter 6. The correction is calculated using two approaches: a phenomenological one and a microscopic one. The former approach is quite qualitative and yields an analytical result, whereas the latter one is more quantitative but leads to complicated integrals. In the end of this chapter we compare both approaches in order to check the validity of the phenomenological approach. Eventually, the weak localization correction is discussed extensively in chapter 7.

## 2. Conductivity

The main goal of this thesis is to calculate the conductivity for a specific model, so it is instructive to start with conductivity in general. Conductivity is a measure for the quality of electron transport. In a metal, the atoms are ordered in a crystalline lattice and we know from Bloch's theorem, that we can find an exact eigenstate for the electrons in a periodic potential. In this state, the electrons don't scatter off the potential and therefore move undisturbed, so the resistivity is zero and the conductivity is infinite.

Experiment tells us that most systems exhibit a finite conductivity, so something cannot be right with our picture. In fact, there are two causes of a finite conductivity: Interaction and disorder. Electron-electron and electron-phonon interactions lead to scattering of the electrons which consequently results in a finite conductivity. In this chapter we concentrate on the role of disorder. The lattice always contains some impurities or vacancies, which destroy the periodicity of the lattice and the potential. So the Bloch state isn't an eigenstate anymore, electrons can scatter and one gets a finite conductivity.

This picture was used by Drude to calculate the conductivity of a solid. He described the electrons as a gas and used kinetic theory. Drude assumed that all electrons scatter over and over again on randomly distributed ions, so electron transport can be treated as *diffusive* transport. By this means, Drude introduced a relaxation time  $\tau$ , which is the time between 2 scattering events and ended up with his well known formula

$$\sigma_D = \frac{ne^2\tau}{m}, \quad (2.1)$$

where  $n$  is the number of electrons per unit cell,  $e$  is the electric charge and  $m$  is the mass of the electron. An equivalent form of the Drude formula can be given by means of the Einstein relation

$$\sigma_D = e^2\nu D \quad (2.2)$$

with the density of states  $\nu$  and the diffusion coefficient  $D = v_f^2\tau$ . The Einstein relation is helpful in later chapters, when we turn to the case of 1D systems.

This rather simple formula has turned out to be very successful in the explanation of the conductivity. Still, it is a classical theory, so it does not cover quantum mechanical effects.

## 2.1. Disorder

We start by looking at the role of disorder in solids. This section is meant to give a brief overview, the detailed calculation can be found in various textbooks like e.g. [8] and [11].

Suppose we have  $n_{imp}$  impurities in our solid, each sitting on a rigid position  $\mathbf{R}_i$  and exhibiting a potential  $\mathcal{U}(\mathbf{x})$ , so the total potential reads

$$U(\mathbf{x}) = \sum_j \mathcal{U}(\mathbf{x} - \mathbf{R}_j). \quad (2.3)$$

The Fourier transform of the single potential is given by  $u(\mathbf{q}) = \int d^3x \mathcal{U}(\mathbf{x}) e^{-i\mathbf{q}\mathbf{x}}$ . Now suppose we have a given distribution of the impurities and electrons can scatter on every single one. Omitting interaction one can write down the full Greens function in a diagrammatic way:

Crosses denote the impurities where the scattering takes place. Note that impurities can change momentum, but conserve frequency. It is also worth mentioning that electrons can scatter multiple times on the same impurity, so the crosses need not denote different impurities.

The notation so far is valid when we know the distribution of the impurities. However, the impurities are randomly distributed in the solid, so it is instructive to average over all impurity positions. The simplest diagram

yields zero upon averaging over the impurity positions. However, when we look at the double scattering event on one impurity

we notice a magnificent fact: upon averaging over impurity positions momentum becomes conserved. Disorder becomes comparable to a 2-particle interaction and one can write down the full Greens function

With this definition of the self-energy  $\Sigma$  one finds

$$\Sigma(i\omega_n) = -i\frac{1}{2\tau}\text{sgn}(\omega_n). \quad (2.4)$$

Note that the self-energy is purely imaginary and the sign depends only on the Matsubara frequency. Using this self-energy we can write down the Matsubara Greens function

$$\begin{aligned} G(k, \omega_m) &= (i\omega_m - \epsilon(k) - \Sigma(i\omega_m))^{-1} \\ &= \left( i\omega_m - \epsilon(k) + i\frac{1}{2\tau}\text{sgn}(\omega_n) \right)^{-1}. \end{aligned} \quad (2.5)$$

The scattering time  $\tau$  is given by

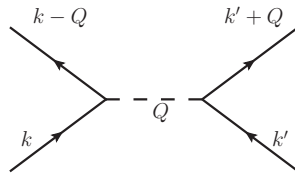
$$\tau^{-1} = 2\pi n_{imp} N(0) \overline{u_0^2}, \quad (2.6)$$

where  $N(0)$  is the density of states at the Fermi energy and  $\overline{u_0^2}$  is the angular average of the impurity scattering potential

$$\overline{u_0^2} = \int \frac{d\Omega_{\mathbf{k}'}}{4\pi} |u(\mathbf{k} - \mathbf{k}')|^2 = \frac{1}{2} \int_{-1}^1 d\cos\Theta |u(\Theta)|^2. \quad (2.7)$$

This result is obtained by the simplest self-energy possible, but calculations show that higher order contributions yield only small corrections to the self-energy.

As already mentioned disorder scattering acts as a 2-particle interaction after averaging over all impurity positions. In this sense one can write down a scattering diagram



with strength

$$\frac{1}{L^d} \langle |u(\mathbf{q})|^2 \rangle = \frac{1}{2\pi\rho\tau}. \quad (2.8)$$

## 2.2. Quantum mechanical approach for the conductivity

We now want to derive the conductivity by using quantum field theory (details may be found in [8] and [11]). Using this formal approach we are able to cover some properties of the conductivity that were not accounted in Drudes theory. However, we will also see that Drudes classical picture of diffusive motion is still correct.

To calculate the conductivity we use Linear Response Theory. In this theory, one calculates the effect of a perturbation to an observable in linear order, the proportionality coefficient is called the susceptibility. The conductivity can be calculated by looking at the correction to the electric current when applying an external electromagnetic field. This leads us to the well known Kubo-formula for the conductivity:

$$\mathbf{j}(q) = \sigma(q)\mathbf{E}(q), \quad (2.9)$$

$$\sigma^{\alpha\beta}(q, \omega) = \frac{i}{\omega} \left\{ \frac{ne^2}{m} \delta^{\alpha\beta} - i \langle T j^\alpha(q) j^\beta(-q) \rangle \right\}, \quad (2.10)$$

where  $\omega$  is the frequency and  $\mathbf{j}$  is the current operator given by

$$j^\alpha(q) = \sum_k e \frac{k^\alpha}{m} \Psi_{k-q/2}^\dagger \Psi_{k+q/2}. \quad (2.11)$$

The current-current-correlator can be written in a diagrammatic way as depicted in figure 2.1. The interaction lines in the diagrams are due to scattering of impurities. The diagrams can be ordered in 2 general classes: The ones with no crossed impurity line (line 2 in figure 2.1) and the ones with fully crossed impurity lines (line 3). The fully crossed diagrams are reduced by a factor of  $\mathcal{O}((kfl)^{-1})$  due to momentum restrictions. Of course there exists a variety of other diagrams, but this categorization is very common since it captures the essential ones. For example, some diagrams can be constructed using Diffuson vertex corrections (this will follow in this section).

When one starts calculating the different diagrams, it turns out that the simplest diagram with no impurity line is already sufficient to cover the Drude conductivity. The diagrams

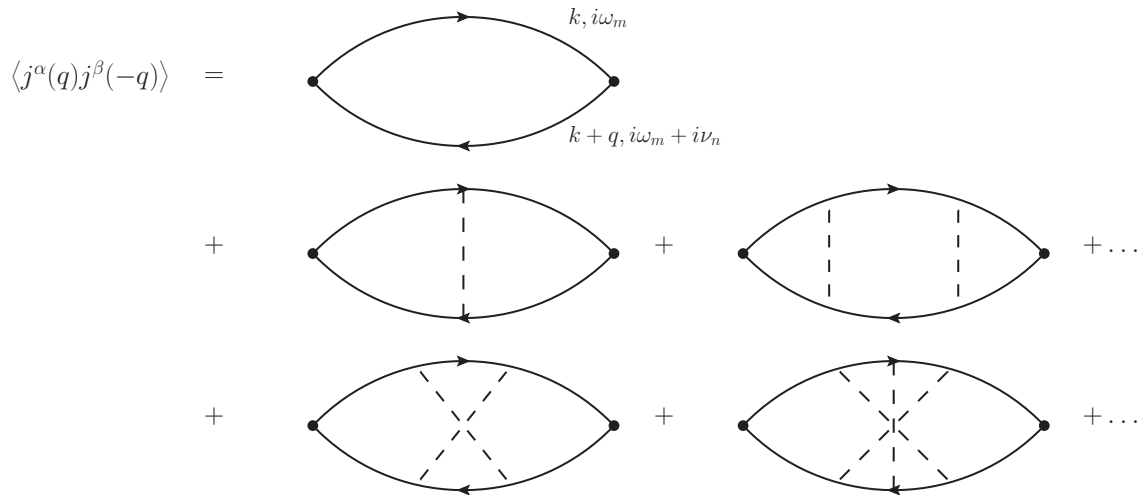


Figure 2.1.: Diagrammatic expansion of the current-current correlator. The left vertex is accounted by a factor of  $ek^\alpha/m$ , the right one by a factor of  $ek^\beta/m$

with no crossed impurity lines cover the scattering behaviour of the impurities and lead to a replacement of the scattering time  $\tau$  with the transport time  $\tau_{tr}$ . This renormalization represents the fact that low angle scattering does not affect conductivity. This kind of diagrams is well-known and the sum over all non-crossed diagrams is called Diffuson, we will account that later. The last set of diagrams, the fully crossed ones, leads to a quantum mechanical correction to the conductivity, the weak localization, which will be explained in a separate section. The collection of the fully crossed diagrams is similar to the Diffuson and is known as the Cooperon.

### 2.2.1. Drude Conductivity

We now look at the current-current correlator in detail. We already mentioned the different parts of the correlator and start with the simplest one, the simple bubble without impurity lines, but with factors  $ek^\alpha/m$  attached to the vertices. After sending the external momentum  $\mathbf{q} \rightarrow 0$ , one finds after some calculation

$$\text{Bubble Diagram} = \frac{ne^2}{m} \frac{1}{\tau^{-1} - i\omega}, \quad (2.12)$$

which is exactly the Drude conductivity for arbitrary frequency  $\omega$ .

### 2.2.2. Diffuson

The second part of the diagrammatic expansion are the bubbles including non-crossed impurity lines. These very general diagrams are known as Diffuson and can be calculated in a self-consistent way:

$$\begin{aligned} \text{Diagram 1} &= \text{Diagram 2} + \text{Diagram 3} + \text{Diagram 4} + \dots \\ &= \text{Diagram 5} + \text{Diagram 6} \end{aligned} \quad (2.13)$$

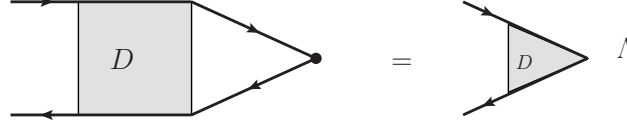
This equation can also be written as

$$D_{p_1, p_2, q} = 1 + \sum_{\mathbf{p}} G_{\mathbf{p}+\mathbf{q}} G_{\mathbf{p}} D_{p, p_2, q}, \quad (2.14)$$

assuming the disorder potential is unity. One can solve this self consistent equation and gets

$$D(\omega, q) = \frac{1}{-i\omega + Dq^2} \quad (2.15)$$

with the diffusion coefficient for 3 dimensions  $D = \frac{1}{3}v_f^2\tau_{tr}$ . (2.15) is also the solution of the diffusion equation  $(-\partial_\tau + D\nabla^2)D(\mathbf{r}, \tau) = \delta^d(\mathbf{r})\delta(\tau)$ , therefore the name Diffuson. In closed loops, the Diffuson can be treated as a vertex correction by closing the legs of it at one side



$$(2.16)$$

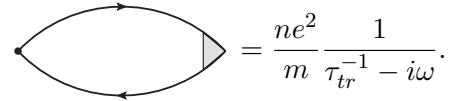
which yields a renormalized vertex

$$\Lambda^\alpha = \frac{-i\omega + \tau^{-1}}{-i\omega + \tau_{tr}^{-1}} \quad (2.17)$$

with a renormalized relaxation time, namely the transport time  $\tau_{tr}$ ,

$$\tau_{tr}^{-1} = 2\pi n_{imp} N(0) \overline{|u(\Theta)|^2 (1 - \cos \Theta)}. \quad (2.18)$$

The transport time takes the anisotropic scattering off the impurities into account, for isotropic scattering  $\tau = \tau_{tr}$  holds. The vertex  $\Lambda$  leads just to a renormalization of the relaxation time  $\tau$  in the Drude conductivity,

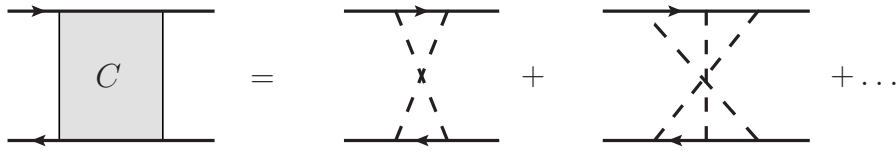


$$(2.19)$$

Eq. (2.18) shows that low-angle scattering is suppressed in  $\tau_{tr}$ , so conductivity is dominated by high-angle scattering.

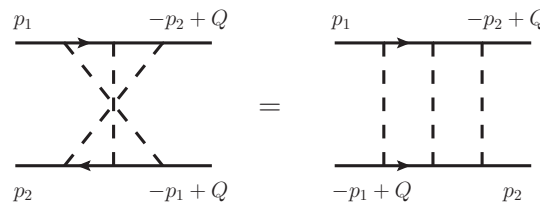
### 2.2.3. Cooperon

We now have a short look at the maximally crossed diagrams in the third line of figure 2.1. These diagrams are also very general and the whole set is called Cooperon.



$$(2.20)$$

In order to write down the Cooperon, one has to perform a little trick: switching the direction of the lower lines leads to a 'decrossing' of the diagrams:



$$(2.21)$$

Using the uncrossed diagrams, one can write down a self-consistent equation similar to eq. (2.13) and gets

$$C(\omega, q) = \frac{1}{-i|\omega| + Dq^2}. \quad (2.22)$$

These diagrams also contribute to the conductivity, but due to momentum restrictions these diagrams are smaller by a factor of  $\mathcal{O}((k_f l)^{-1})$ . The calculation of this correction is quite difficult (as explained in [2]), but one ends up with some interesting physical behaviour: These diagrams tend to decrease conductivity, but due to the small factor of order  $\mathcal{O}((k_f l)^{-1})$  this effect is only seen at low enough temperatures. A phenomenological explanation of this effect (which is called *weak localization*) can be given, this is done in the next section.

### 2.3. Weak Localization

Including disorder in a system can also be seen as including a new type of interaction, and like every interaction, disorder can lead to new kinds of collective phenomena. Let's suppose that an electron scatters on different impurity sites and after some time it returns to the starting point. On his way from impurity  $i$  to impurity  $i + 1$  the wavefunction of the electron collects a phase of  $\exp[ik(\mathbf{R}_{i+1} - \mathbf{R}_i)]$ , where the  $\mathbf{R}_j$  are the positions of the impurities. The total phase the electron acquires is  $\exp[i\phi_1]$ . However, the electron can also perform a different path, scattering on different impurities. After returning to the starting point, this path would yield a phase of  $\exp[i\phi_2]$ . We can now calculate the return probability to the starting point using the two paths:

$$|A_1 + A_2|^2 = |A_1|^2 + |A_2|^2 + 2|A_1 A_2| \cos(\phi_1 - \phi_2) \quad (2.23)$$

The return probability consists of the two single amplitudes and an interference term. Now suppose we take every possible closed way into account, yielding a lot of interference terms. Since these interference terms depend strongly on the path, the sum over all of them yields zero on the average. This means that the return probability is just given by the single amplitudes.

Now imagine 2 paths as depicted in fig. 2.2. The 2 paths follow the same impurities, but in different order. In this sense, the second path is just the time-reversed first path. It is clear that both paths acquire the same phase, so the phase difference vanishes  $\phi_1 - \phi_2 = 0$ . Since this relation holds for every impurity configuration, these paths survive the averaging over impurity positions. In consequence, such configurations lead to an enhanced return probability and the electrons become more localized.

The time-reversed path visits the impurities in opposite order than the electron on the regular path, so processes like the one in fig. 2.2 are described by diagrams like fig. 2.3. These kind of diagrams have been discussed in the last section and the whole set of them is called Cooperon.

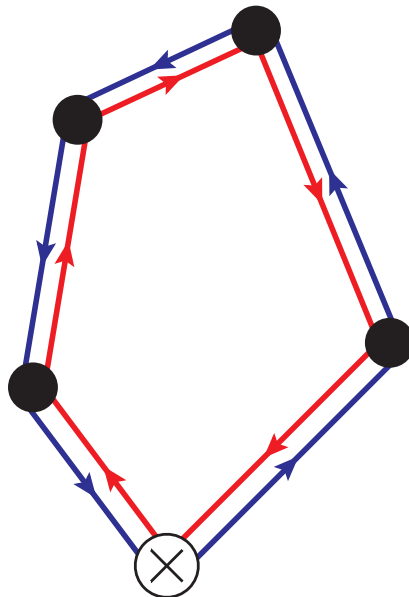


Figure 2.2.: Illustration of two paths scattering off the same impurities. Blue path is the time-reversed red path.

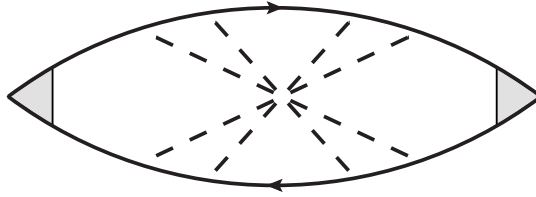


Figure 2.3.: Conductivity bubble containing 4 crossed impurity lines. Processes like the one in fig. 2.2 are described by such diagrams.

The loops like in fig. 2.2 can in general become arbitrarily large, which leads full localization at any temperature in low dimensional systems. This is not true anymore when other couplings like electron-electron or electron-phonon interactions are included. These additional couplings lead to inelastic scattering effects and destroy coherence, this effect is called *dephasing*. The dephasing is accounted in a phenomenological way by introducing a new length  $l_\phi$ , which acts as a cutoff in the integrals. After traveling a length of  $l_\phi$ , coherence is destroyed by inelastic scattering and the electron cannot interfere constructively anymore with the one on the time reversed path.

Since this effect tends to localize electrons, it also decreases conductivity. When temperatures are high enough, one can safely neglect the effect of weak localization, but on lower temperatures it becomes relevant. There are two ways to modify the strength of weak localization: The dephasing length  $l_\phi$  can be modified by tuning the temperature or by applying a magnetic field. Magnetic fields break time reversal symmetry, so the two paths do not collect the same phase anymore and the effect of weak localization disappears. Since weak localization is directly connected to the conductivity, one observes magnetoresistance.

The phenomenon of localization strongly depends on the dimensionality of the system. In a 3D system, a specific amount of disorder is needed to get localization at all. The situation is profoundly different in lower dimensional systems. In 2D as well as in 1D systems electrons become localized as long as an arbitrary small amount of disorder is included in the system. For 1D systems the localization is even more pronounced than in 2D. This was a result of the scaling theory, introduced by the ‘‘Gang of Four’’, Abrahams, Anderson, Licciardello and Ramakrishnan [1].



### 3. 1D-systems

One dimensional systems are a fascinating field of physics. They exhibit exotic effects which cannot be seen in higher dimensional system, but furthermore they have led to very sophisticated theoretical methods. In this chapter we introduce some of these phenomenons and discuss the basic methods which are used to tackle these problems. This chapter intends to give a brief overview, the interested reader might consider [16], [12] and [18] (This chapter is based on [16] as long as no other source is given).

Talking about system with one spatial dimension naturally gives rise to the question: How can these systems be realized in experiment? Even an atom has an extension in all 3 dimensions, so how can something one dimensional be constructed? The answer is that one has to use a trick, namely, quantum mechanics. When the lateral extension of an object is so small that it only exhibits few eigenstates in this direction, the object can be treated as effectively one-dimensional. Examples for effective 1D systems are quantum wires [5, 23, 33] and carbon nanotubes [7]. There also exist materials with strong anisotropic hopping (e.g.  $\text{PrBa}_2\text{Cu}_4\text{O}_8$  [14, 29]). These materials exhibit strong hopping in one direction and weak hopping in the other directions, so electrons are also confined to a quasi 1D-system.

### 3.1. Phenomenology of 1D-systems

When one starts treating a specific problem in quantum physics, it is mostly quite easy to solve it neglecting any interaction. Upon turning on interaction, the problem becomes usually much more difficult. In the low-energy-limit, interaction excites an electron sitting just below the Fermi surface, so afterwards it's just above the Fermi surface and a hole remains inside. These excitations are dressed by density fluctuations, and it was Landau's idea to treat the fermionic excitations plus the fluctuations as single quasiparticles. These quasiparticles can be considered as essentially free, so we are back at the noninteracting problem.

This picture is only correct as long as the excitations can be described as quasiparticles, that is, when the lifetime of the excitations is long enough. Landau showed that the lifetime can be estimated by a simple phase space argument: excitations just above the Fermi surface do not have much phase space to scatter in, so the closer to the Fermi surface one gets, the more divergent becomes the lifetime:

$$\tau^{-1} \propto (\epsilon - E_f)^2. \quad (3.1)$$

This whole construct of noninteracting quasiparticles is known as *Fermi Liquid*. A more quantitative discussion of this model is given e.g. in [32]. One can show that interactions lead to a renormalized mass in the kinetic energy,  $m^*$ , and most physical quantities can be obtained by the replacement  $m \rightarrow m^*$ . Since the estimate of the lifetime of the quasiparticles was performed by a simple phase space argument, we are not even restricted to weak interaction. The great strength of Fermi Liquid theory is, that it is still valid at very strong couplings.

Let's now turn to the situation in one dimension. Suppose interaction pushes an electron towards a specific direction. As seen in fig. 3.1, interactions in 2 or higher dimensions can lead to single particle excitations. In one dimension, however, excited electrons try to push neighbouring electrons away simply because they cannot evade each other. It is obvious that single particle excitations cannot exist and only collective modes can emerge from interaction. As a consequence, Fermi Liquid theory is no longer applicable and we have to introduce a new concept called Luttinger Liquid. Luttinger Liquid was designed to deal with the collective interactions in 1D and will be explained in the next section.

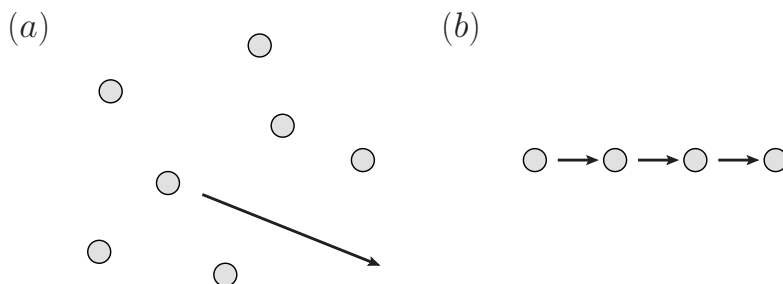


Figure 3.1.: (a) Interaction in 2 or 3 dimensions. The excitation can be seen as single particle excitation. (b) Interaction in 1 dimension. The electrons cannot evade each other, so only collective excitations are possible.

### 3.2. Methods in one dimension

We already know that we cannot use Fermi Liquid theory anymore, so we need a new way to treat problems in one dimension. We start by restricting ourselves to low energy physics, that is, to excitations in the vicinity of the Fermi surface. This assumption is reasonable because the Fermi energy is about  $10000K$  for normal metals, whereas one typically works at temperatures of order  $1 - 100K$ . For this reason the spectrum is approximated linearly in the vicinity of the Fermi points, as presented in fig. 3.2. This linearization is extended over the whole  $k$ -space for mathematical reasons, the resulting model is called Tomonaga-Luttinger-model. A linear spectrum is equivalent to a constant density of states, which is a pretty common approximation. Note that the linearization is done at two points, at  $+k_f$  and  $-k_f$ . We therefore get 2 branches in the spectrum, one linear band with Fermi velocity  $+v_f$  and one with  $-v_f$ . In consequence, we introduce a new quantum number, the chirality, which tells us on which branch of the spectrum we are. Electrons with positive Fermi velocity are called right-movers (chirality R), the ones with negative Fermi velocity are called left-movers (chirality L).

Let's now turn to the interaction in the Tomonaga-Luttinger-model. In second quantization one can write the two-particle interaction as

$$H_{int} = \frac{1}{2\Omega} \sum_{k,k',q} V(q) c_{k+q}^\dagger c_{k'-q}^\dagger c_{k'} c_k. \quad (3.2)$$

In the linearized spectrum the interaction can be categorized into 3 different interaction types (see fig. 3.2):  $g_1$ ,  $g_2$  and  $g_4$ . This categorization is also known as *g-ology*.  $g_2$  and  $g_4$ -processes leave the electrons on their branch, this kind of interaction is called forward scattering. The  $g_1$ -process switches the chirality of the electrons, this behaviour is called backscattering. Note that in the absence of spin  $g_1$ - and  $g_2$ -processes are the same because the particles are identical.

The  $g_2$  and  $g_4$ -processes are coupled to the  $q \sim 0$  matrix element, whereas the  $g_1$  term is coupled to the one with  $q \sim 2k_f$ . It is a common approximation to neglect the  $q \sim 2k_f$ -term, because the matrix element is usually much smaller. This means that we omit backscattering in the interaction and keep only the forward scattering processes. This model (omitting backscattering) is called Luttinger Liquid, the model with relevant backscattering is called Luther-Emery Liquid (this results in a gap opening in the spin channel). Omitting backscattering leads also to much simpler calculations and results are obtained in a very straightforward way. One crucial result is, that all fermion bubbles with more than two interaction lines vanish, this means that RPA has become exact in this model (see [13]). When looking at the Fermi velocity, one notes that it becomes renormalized by interaction and, more remarkably, separates into 2 different velocities when spin

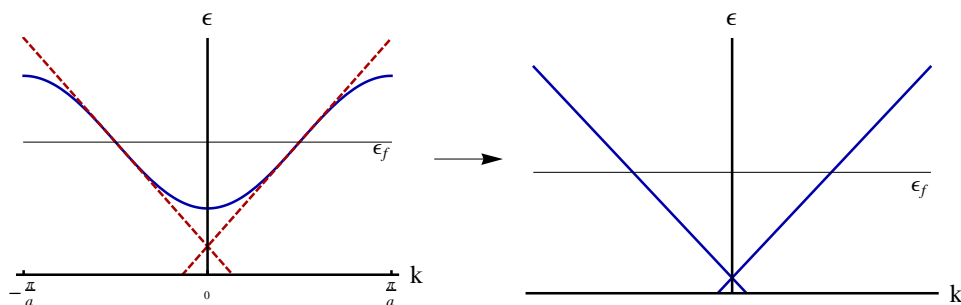


Figure 3.2.: Linearization of the spectrum in the vicinity of the Fermi points.

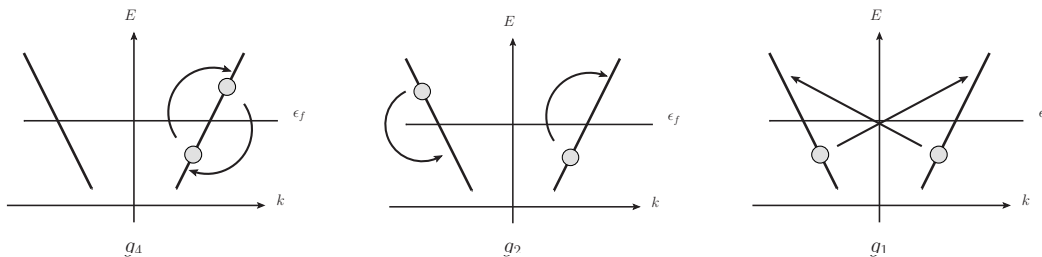


Figure 3.3.: g-ology-based interaction in band space.  $g_4$  and  $g_2$  processes leave the electrons on their branch (forward scattering),  $g_1$  process switches the branches (backscattering)

is included. This means that spin excitations move with a different velocity than charge excitations, this phenomenon is called spin-charge-separation.

The calculations so far have been done in the very beginning by Dzyaloshinskii and Larkin [13] in the standard fermion language. We have already discussed, that one dimensional systems don't exhibit single particle excitations, but only collective modes. These modes can be seen as density fluctuations, therefore they behave as bosons. Having said this, fermionic language isn't the best one to suit one dimensional problems. Indeed, a mapping of the form

$$\Psi(x) \sim e^{i \int^x dx' \rho(x')} \quad (3.3)$$

can be found to transform the Hamiltonian from fermionic to bosonic language.  $\Psi$  is a fermionic operator,  $\rho$  is the particle density. This transformation leads to a Hamiltonian of the form

$$H \simeq \sum_{p \neq 0} v_f |p| b_p^\dagger b_p, \quad (3.4)$$

where  $b_p$  is a bosonic operator. The given formulas aren't exact ones, they are just presented to give an impression of the technique, which is called *Bosonization*. The full derivation is quite difficult, but in the end one gets formulas which can be used easily. Bosonization recovers previous results like spin-charge-separation, but furthermore it exhibits interesting features like a power-law behaviour of the correlation functions.

## 4. Functional Bosonization

We already know that we have to use special techniques to treat one-dimensional problems. In the last chapter we introduced a technique called bosonization, which accounts the collective behaviour of interactions. In this chapter we introduce a slightly different approach called Functional Bosonization. This approach is more flexible than standard bosonization since one bosonizes only by part. This section is meant to give a short derivation of this method, the first part contains a general derivation, in the second part we introduce a diagrammatic technique to treat interaction.

### 4.1. General Derivation

Functional Bosonization was derived by different groups, it was suggested in 1976 by Fogedby [15] and fully elaborated by Lee and Chen [22] twelve years later. We follow the method of Yurkevich [39], who used a Hubbard-Stratonovich-Transformation to treat the interaction.

We start with a general Hamiltonian in one dimension:

$$H = \frac{1}{2m} \int dx \partial_x \Psi^\dagger(x) \partial_x \Psi(x) + \frac{1}{2} \int dx dx' \Psi^\dagger(x) \Psi^\dagger(x') V_0(x-x') \Psi(x') \Psi(x), \quad (4.1)$$

where  $V_0$  is the electron-electron interaction, usually one uses the screened Coulomb interaction. It is known that the Greens function can be written in terms of a functional integral:

$$G(x, \tau; x', \tau') = \frac{\int \mathcal{D}\psi \mathcal{D}\psi^* \psi(x, \tau) \psi^*(x', \tau') \exp\{-\mathcal{S}[\psi, \psi^*]\}}{\int \mathcal{D}\psi \mathcal{D}\psi^* \exp\{-\mathcal{S}[\psi, \psi^*]\}}. \quad (4.2)$$

The action  $\mathcal{S}[\psi, \psi^*]$  is given by

$$\begin{aligned} \mathcal{S}[\psi, \psi^*] &= \int dx d\tau \psi^*(x, \tau) [\partial_\tau + \xi] \psi(x, \tau) \\ &\quad + \frac{1}{2} \int dx dx' d\tau \psi^*(x, \tau) \psi^*(x', \tau) V_0(x-x') \psi(x', \tau) \psi(x, \tau) \\ &= \mathcal{S}_{kin}[\psi, \psi^*] + \mathcal{S}_{int}[\psi, \psi^*], \end{aligned} \quad (4.3)$$

where  $\xi = -(2m)^{-1}\partial_x^2 - \mu$  is the kinetic energy operator, renormalized by the chemical potential  $\mu$ . The  $\psi$ 's are Grassmann functions, which are anti-periodic in  $\tau$  with period  $\beta = T^{-1}$ :

$$\psi(\tau + \beta) = -\psi(\tau). \quad (4.4)$$

As mentioned before interactions between the electrons result in collective modes, which have bosonic character. So it is straightforward to introduce a bosonic field in the interaction and to get rid of the four-fermion-interaction. This is done by means of a Hubbard-Stratonovich transformation [34], which leads us to

$$\exp[-\mathcal{S}_{int}] = \frac{\int \mathcal{D}\phi \exp[-\frac{1}{2}\phi V_0^{-1}\phi + i\phi\psi^*\psi]}{\int \mathcal{D}\phi \exp[-\frac{1}{2}\phi V_0^{-1}\phi]}, \quad (4.5)$$

where we used the short handed notation

$$\phi V_0^{-1}\phi = \int dx dx' d\tau \phi(x, \tau) V_0^{-1}(x - x') \phi(x', \tau), \quad (4.6a)$$

$$\phi\psi^*\psi = \int dx d\tau \phi(x, \tau) \psi^*(x, \tau) \psi(x, \tau). \quad (4.6b)$$

The advantage is that we are only left with a bilinear combination of the fermionic  $\psi$ -fields, whereas the interaction  $V_0$  is now coupled to a auxiliary  $\phi$ -field. But there is also an obvious disadvantage, namely the additional integration over the  $\phi$ -field. One can easily check that the  $\phi$ -fields 'replaced' products of two fermionic fields  $\psi^*(x, \tau)\psi(x, \tau)$ , therefore the  $\phi$ -fields should be bosonic. Inserting Gaussian integrals over the fermionic Grassmann fields leads to a new representation of the Greens function. The full Greens function can now be written as an average over the auxiliary  $\phi$ -field:

$$G(x, \tau; x', \tau') = \left\langle \tilde{G}(x, \tau; x', \tau'; [\phi]) \right\rangle_\phi = \frac{\int \mathcal{D}\phi \tilde{G}(x, \tau; x', \tau'; [\phi]) \exp[-\mathcal{S}[\phi]]}{\int \mathcal{D}\phi \exp[-\mathcal{S}[\phi]]}, \quad (4.7)$$

where the action is given by

$$\mathcal{S}[\phi] = \frac{1}{2}\phi V_0^{-1}\phi - Tr \ln[\partial_\tau + \xi - i\phi] \quad (4.8)$$

and the auxiliary Greens function  $\tilde{G}$  is obtained from the equation

$$(\partial_\tau + \xi - i\phi(x, \tau)) \tilde{G}(x, \tau; x', \tau'; [\phi]) = \delta(x - x')\delta(\tau - \tau'). \quad (4.9)$$

With this given framework we can generally compute the Greens function for an arbitrary bosonic field  $\phi$ , the interaction  $V_0$  is still included in the action  $\mathcal{S}$  and therefore taken into account in the averaging over the  $\phi$  field.

In order to simplify the equations above we turn to the case of a linearized spectrum. Neglecting backscattering by electron-electron interaction leads to two Greens functions, one for right movers and one for left movers. The important difference to the general model is that the kinetic energy can be written in terms of a single derivative:

$$\xi = \mp i v_f \partial_x, \quad (4.10)$$

where the different signs denote different branches. So the equation for the auxiliary Greens function reads

$$(\partial_\tau \mp iv_f \partial_x - i\phi(x, \tau)) \tilde{G}_\pm(x, \tau; x', \tau'; [\phi]) = \delta(x - x') \delta(\tau - \tau'). \quad (4.11)$$

Since one is only left with a single derivative, the noninteracting and the interacting part in the Greens function can be split by introducing a new field  $\Theta(x, \tau)$

$$\begin{aligned} \tilde{G}^R(x, \tau; x', \tau'; [\phi]) &= g^R(x - x', \tau - \tau') e^{i\Theta(x, \tau) - i\Theta(x', \tau')}, \\ \tilde{G}^L(x, \tau; x', \tau'; [\phi]) &= g^L(x - x', \tau - \tau') e^{i\Theta^*(x, \tau) - i\Theta^*(x', \tau')}, \end{aligned} \quad (4.12)$$

where the  $\Theta$ -field should be derived from

$$(\partial_\tau - iv_F \partial_x) \Theta(x, \tau) = \phi(x, \tau) \quad (4.13)$$

and the  $g^{R/L}(x, \tau)$  are the free Greens functions

$$g^{R/L}(x, \tau) = \mp \frac{iT}{2v_f} \sinh^{-1} \left[ \pi T \left( \frac{x}{v_f} \pm i\tau \right) \right]. \quad (4.14)$$

Since the free Greens functions do not contain any  $\phi$  fields, the averaging from equation (4.7) affects only the exponentials containing the  $\Theta$  functions. The averaging can be done using the equation

$$\left\langle e^{i \sum_j A_j \phi(x_j)} \right\rangle_\phi = e^{-\frac{1}{2} \left\langle [\sum_j A_j \phi(x_j)]^2 \right\rangle_\phi}. \quad (4.15)$$

This equation holds for a quadratic Hamiltonian and can be found for instance in [16]. Using this expression we find for the right moving Greens function

$$\begin{aligned} \left\langle \tilde{G}^R(x, \tau; [\phi]) \right\rangle_\phi &= g^R(x, \tau) \exp \left[ -\frac{1}{2} \left\langle [\Theta(x, \tau) - \Theta(0, 0)]^2 \right\rangle_\phi \right] \\ &= g^R(x, \tau) \exp[-B_{RR}(x, \tau)]. \end{aligned} \quad (4.16)$$

The explicit form of the  $B_{\mu, \nu}$ -correlators can be looked up in Appendix C.

## 4.2. Diagrammatic Technique

In the previous section we treated the single-particle Greens function in the functional bosonization approach, but the quantities we want to calculate are observables, or in our case, closed fermionic loops. This loops can contain scattering off disorder, interaction is already accounted in the  $\Theta$ -fields. This question was treated by Gornyi, Mirlin, Polyakov and Yashenkin in [19] and [37]. This section is meant to give a brief introduction in their way of treating the problem, the detailed calculation can be found in the cited articles.

The idea of their work is the following: One starts with the general definition of the free Greens function as the average over a bilinearform of the free fermion field  $\Psi(x, \tau)$ :

$$G(x - x', \tau - \tau') = - \left\langle T_\tau \Psi(x, \tau) \Psi^\dagger(x', \tau') \right\rangle. \quad (4.17)$$

The interaction is included by performing the gauge transformation

$$\Psi_\mu(x, \tau) \longrightarrow \Psi_\mu(x, \tau) e^{i\Theta_\mu(x, \tau)}, \quad (4.18)$$

where  $\mu$  is chirality. This gives immediately the same result as in (4.12). Since the fermionic  $\Psi$ -operators denote somehow the start- and endpoints of the propagator, interaction is now included in these via a phase factor. These phase factors can be written as interaction lines attached to the vertices and the lines are getting connected by averaging over the  $\Theta$  field (see fig. 4.1). The averaging yields a correlation function

$$B_{\mu\nu}(x, \tau) = \langle [\Theta_\mu(0, 0) - \Theta_\mu(x, \tau)] \Theta_\nu(0, 0) \rangle, \quad (4.19)$$

which restores eq. (4.16). Inserting all parameters yields for the spinless case

$$G^R(x, \tau) = - \frac{i}{2\pi u} \frac{\pi T}{\sinh[\pi T(x/u + i\tau)]} \left\{ \frac{\pi T/\Lambda}{\sinh[\pi T(x/u + i\tau)]} \frac{\pi T/\Lambda}{\sinh[\pi T(x/u - i\tau)]} \right\}^{\tilde{y}/2} \quad (4.20)$$

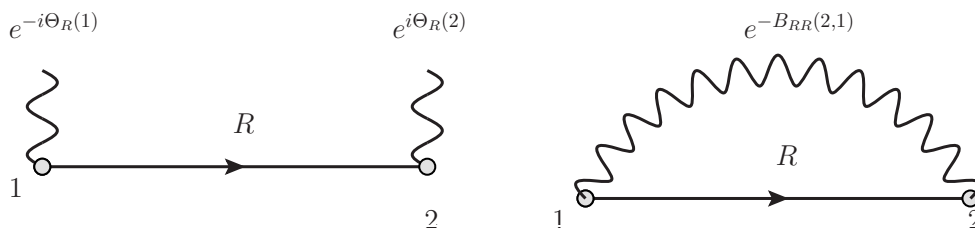


Figure 4.1.: Greens function for a right mover;  $1=(x_1, \tau_1)$ ,  $2=(x_2, \tau_2)$ ; left: Propagator with phase factors attached on vertices; right: Propagator with averaged over  $\Theta$  which results in connecting the two phase factors,  $B(2, 1)$  is understood as  $B(x_2 - x_1, \tau_2 - \tau_1)$ .

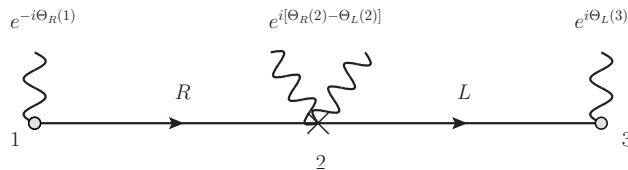


Figure 4.2.: Backscattering of a right moving electron. Each Greens function gets attached by 2 phase factors, one at each space-time-point.

and for the spinful case

$$G^R(x, \tau) = -\frac{i}{2\pi\sqrt{uv_f}} \left\{ \frac{\pi T}{\sinh[\pi T(x/v_f + i\tau)]} \frac{\pi T}{\sinh[\pi T(x/u + i\tau)]} \right\}^{1/2} \times \left\{ \frac{\pi T/\Lambda}{\sinh[\pi T(x/u + i\tau)]} \frac{\pi T/\Lambda}{\sinh[\pi T(x/u - i\tau)]} \right\}^{\tilde{y}/4}, \quad (4.21)$$

where  $y = g/2\pi v_f$  is the dimensionless interaction strength,  $u = v_f\sqrt{1+4y}$  is the renormalized Fermi velocity,  $\Lambda$  is some high-energy cutoff and the exponent  $\tilde{y}$  is given in eq. (C.7). These equations are given in more detail in Appendix C, the whole calculation is found in [19] and [37].

Until now we have just treated the problem of a single propagator, but we are interested in more complicated expressions, especially closed fermionic loops containing scattering off disorder. The diagrammatic technique presented in this section is a convenient method to treat this problem.

Note that in principle interaction and disorder both can scatter forwards and backwards. Interaction is taken into account via the *g-ology* approach explained in 3.2, we already noted there that backscattering is neglected. However, this only holds for interaction-induced scattering, disorder can still scatter forwards and backwards. Since low-angle scattering doesn't affect conductivity, we only consider backward scattering in disorder in our calculations.

For the beginning let's just look at one backscattering vertex (fig. 4.2). In contrast to the Greens function we are left with 4 phase factors to be averaged, so it is not clear how the averaging has to be done. It turns out that the averaging can be done in a quite straightforward way: Every wavy line has to be connected with every other one, yielding several  $B_{\mu\nu}$ -correlators, which have to be added up. In the diagrammatic scheme, this results in a slightly complicated picture depicted in fig. 4.3.

Of course the diagrams become more complicated the more impurity scattering vertices are included. Fortunately it turns out that the averaging can be simplified a lot. In closed loops, the correlators  $B_{\mu\nu}(x, \tau)$  (also given in Appendix C) appear only in one combination:

$$M(x, \tau) = B_{RR}(x, \tau) + B_{LL}(x, \tau) - 2B_{RL}(x, \tau). \quad (4.22)$$

Knowing this factor, the averaging in a closed fermionic loop can be done in a very formal way: For every pair of backscattering vertices at  $(x_N, \tau_N)$  and  $(x_{N'}, \tau_{N'})$  one takes a factor of

$$Q(x, \tau) = \exp[M(x, \tau)] \quad (4.23)$$

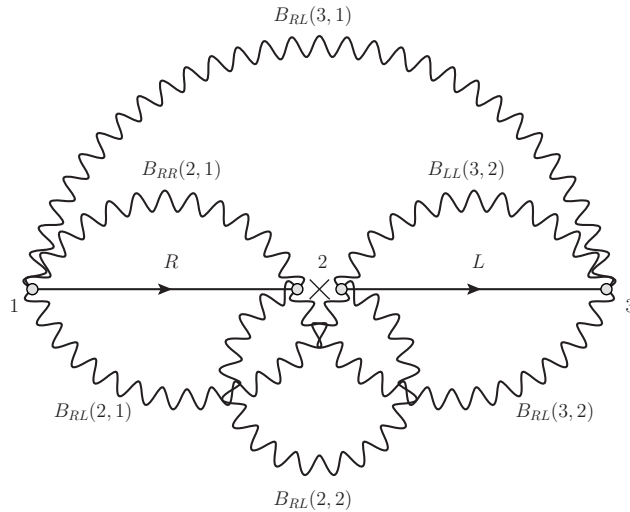


Figure 4.3.: Backscattering of a right moving electron. The averaging over the  $\Theta$  fields is performed, so the phase factors are connected in every possible way.

into account, where  $x = x_N - x_{N'}$  and  $\tau = \tau_N - \tau_{N'}$  or a factor of  $Q^{-1}(x, \tau)$ . The factor depends on the chirality of the incident electrons at the backscattering vertices: If the chiralities are the same, one has to take a factor of  $Q(x, \tau)$ , if they are different, one has to take a factor of  $Q^{-1}(x, \tau)$ , respectively. Note that *every* pair of backscattering vertices contributes. In the case of 4 impurities, for example, the impurity vertex at  $x_1$  has to be averaged with the ones at  $x_2$ ,  $x_3$  and  $x_4$ .

Let's summarize the results of this section. In the beginning we used Functional Bosonization to treat the interaction and we managed to move the electron-electron interaction into an additional phase factor attached to the free Greens function, seen in eq. (4.12). This approach can be used to calculate closed fermionic loops by just averaging over all possible combinations of the phase factors. This results in a factor of  $Q(x, \tau)$  or  $Q^{-1}(x, \tau)$  (given in eq. (4.23)), depending on chirality. So in the very end one is left with free Greens functions and a bunch of  $Q$ - and  $Q^{-1}$ -functions.

## 5. Ladder Model

In this section we introduce the spinless disordered 2-chain ladder model used in this work. We will calculate the dispersion relation of the ladder, as well as the effect of a magnetic field. Moreover, a mapping between the Greens functions in chain space and the ones in band space will be found.

### 5.1. Ladder without magnetic field

We first start without the magnetic field and use the following model:

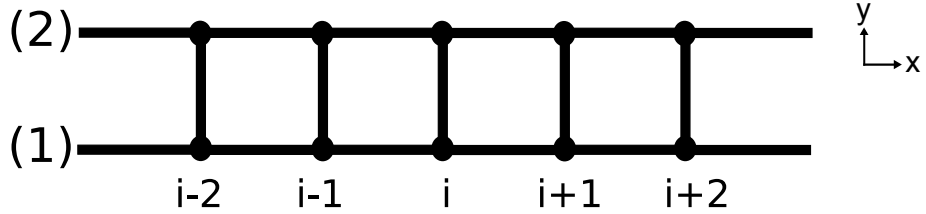


Figure 5.1.: 2-chain-ladder in real space. 1 and 2 denote chain index,  $i$  denotes atom site.

The dots represent atom sites and the lines show the ways the electrons can hop. The ladder is in real space, so we have a length  $a_y$ , the distance between chain 1 and chain 2, and another length  $a_x$  which is the distance between two neighbouring sites on one chain. We can now write down the Hamiltonian

$$H = H_{\text{kin}} + H_{\text{dis}} + H_{\text{int}} \quad (5.1)$$

with

$$H_{\text{kin}} = \sum_i \left[ -t_{\parallel} \left( c_{1,i}^{\dagger} c_{1,i+1} + h.c. \right) - t_{\parallel} \left( c_{2,i}^{\dagger} c_{2,i+1} + h.c. \right) - t_{\perp} \left( c_{1,i}^{\dagger} c_{2,i} + h.c. \right) \right], \quad (5.2a)$$

$$H_{\text{dis}} = \sum_{l,i} V_{l,i}^{\text{dis}} n_{l,i}, \quad (5.2b)$$

$$H_{\text{int}} = \frac{1}{2} \sum_{l,l',i,i'} V_{l,l',i,i'}^{e-e} n_{l,i} n_{l',i'}. \quad (5.2c)$$

Summation indices  $i, i' = 1, 2$  denote chain indices,  $l, l'$  denote atom sites in x-direction.  $t_{\parallel}$  and  $t_{\perp}$  are the hopping parameters for intra- and inter-chain hopping, respectively,  $V^{\text{dis}}$  is a randomly distributed impurity scattering potential and  $V^{e-e}$  is the electron-electron interaction. Disorder and interaction both couple to the particle density  $n_{l,i} = c_{l,i}^{\dagger} c_{l,i}$ .

The kinetic Hamiltonian can be diagonalized with a linear transformation, namely

$$c_{\pm,i} = \frac{1}{\sqrt{2}}(c_{1,i} \pm c_{2,i}). \quad (5.3)$$

The new operators  $c_{\pm,i}$  obey the standard fermion anticommutator relations:

$$\{c_{a,i}, c_{a',i'}\} = 0, \quad \{c_{a,i}^{\dagger}, c_{a',i'}^{\dagger}\} = 0, \quad \{c_{a,i}, c_{a',i'}^{\dagger}\} = \delta_{a,a'} \delta_{i,i'}. \quad (5.4)$$

After this transformation the kinetic Hamiltonian splits up in two parts

$$H_{\text{kin}} = H_{+} + H_{-} \quad (5.5)$$

with

$$H_{\pm} = \sum_i \left[ -t_{\parallel} \left( c_{\pm,i}^{\dagger} c_{\pm,i+1} + h.c. \right) \mp t_{\perp} c_{\pm,i}^{\dagger} c_{\pm,i} \right]. \quad (5.6)$$

This transformation eliminates the hopping between the two chains and separates the problem into two independent parts. To get the band structure, we can now easily transform the Hamiltonian into momentum space using a Fourier transformation:

$$\begin{aligned} H_{\pm} &= \sum_k \left[ -t_{\parallel} c_{\pm,k}^{\dagger} c_{\pm,k} \left( e^{ika_x} + e^{-ika_x} \right) \mp t_{\perp} c_{\pm,k}^{\dagger} c_{\pm,k} \right] \\ &= \sum_k \left[ -2t_{\parallel} c_{\pm,k}^{\dagger} c_{\pm,k} \cos(ka_x) \mp t_{\perp} c_{\pm,k}^{\dagger} c_{\pm,k} \right] \\ &= \sum_k \epsilon_{\pm,k} c_{\pm,k}^{\dagger} c_{\pm,k}, \end{aligned} \quad (5.7)$$

with the given dispersion

$$\epsilon_{\pm,k} = -2t_{\parallel} \cos(ka) \mp t_{\perp}. \quad (5.8)$$

We have shown that the band structure of the 2-chain ladder consists of two cosine-formed bands split by  $\Delta\epsilon = 2t_{\perp}$  (depicted in fig. 5.2). Since the physics happens only in the vicinity of the Fermi energy, we approximate the two bands by a linear model. Although the Fermi velocities of the two bands are in general different, we choose them to be the same in the linear model (fig. 5.3). This assumption is good as long as the Fermi energy does not approach a band minimum. Note that the two bands  $+/-$  are solely defined by their respective Fermi momentum  $k_{f,\pm}$ . An alternative model which also yields linear

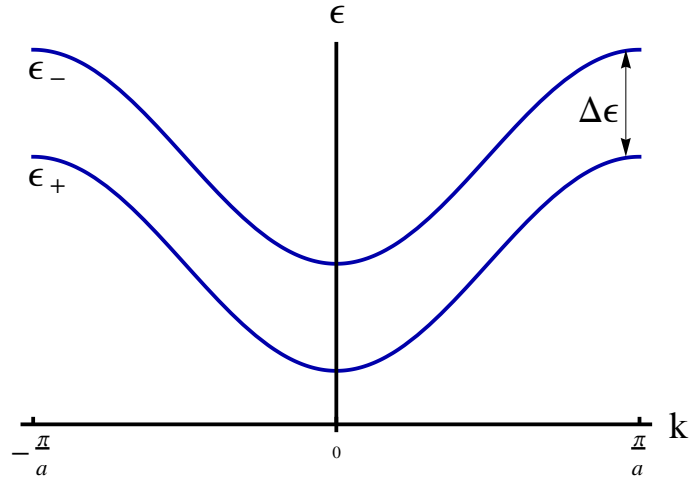


Figure 5.2.: Band structure of the 2 chain model.

bands is that of the continuous ladder. In this specific model, the lattice in x-direction has been omitted, which leads to continuous chains.

We can now write down the retarded Greens function in band space for the linearized model:

$$\begin{aligned} G_j^R(k) &= \frac{1}{\omega - v_f(k - k_{f,j}) + i0}, \\ G_j^L(k) &= \frac{1}{\omega - v_f(-k - k_{f,j}) + i0}. \end{aligned} \quad (5.9)$$

The upper index denotes the right-/left-moving character of the fermions, the lower index  $j = \pm$  denotes band index. The advanced Greens functions are given by the complex conjugate of the retarded ones  $(G_j^{R/L})^*$ .

As discussed in section 2.1, disorder leads to a relaxation time  $\tau$ . We expect this behaviour also in the ladder model, so we account disorder by adding a relaxation time  $\tau$  to the retarded Greens functions:

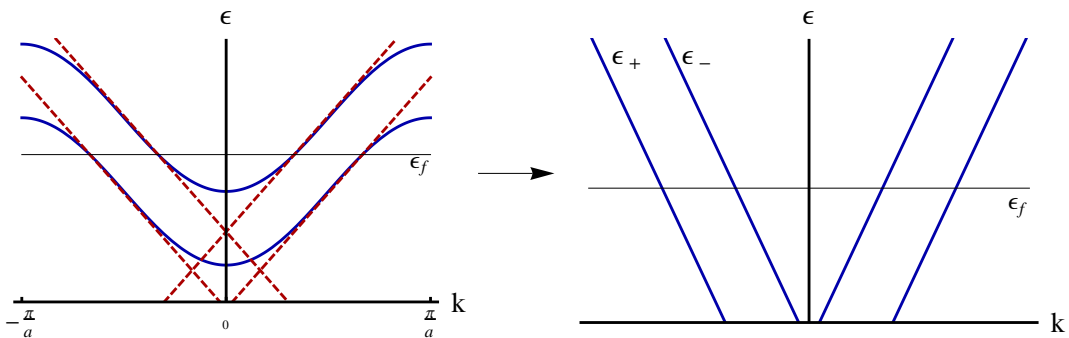


Figure 5.3.: Linearizing the band structure: We use one Fermi velocity for both bands, the only difference between the two bands is then  $k_{f,\pm}$ .

$$\begin{aligned}
G_j^R(k) &= \frac{1}{\omega - v_f(k - k_{f,j}) + i/2\tau}, \\
G_j^L(k) &= \frac{1}{\omega - v_f(-k - k_{f,j}) + i/2\tau}.
\end{aligned} \tag{5.10}$$

The advanced Greens functions are still given by the complex conjugate of the retarded ones  $(G_j^{R/L})^*$ . We have chosen the relaxation times of the two bands to be the same because we expect that the scattering length  $l = v_f\tau$  should be the same in both bands.

The transformation from band to chain basis is known from equation (5.3), inverting the equation leads to the inverse transformation (note that we start directly in momentum space)

$$c_{1,k} = \frac{1}{\sqrt{2}}(c_{+,k} + c_{-,k}), \quad c_{2,k} = \frac{1}{\sqrt{2}}(c_{+,k} - c_{-,k}), \tag{5.11}$$

which leads to the relations

$$\begin{aligned}
G_{1,1}^{R/L}(k) = G_{2,2}^{R/L}(k) = G_{\parallel}^{R/L}(k) &= \frac{1}{2} \left( G_+^{R/L}(k) + G_-^{R/L}(k) \right), \\
G_{1,2}^{R/L}(k) = G_{2,1}^{R/L}(k) = G_{\perp}^{R/L}(k) &= \frac{1}{2} \left( G_+^{R/L}(k) - G_-^{R/L}(k) \right).
\end{aligned} \tag{5.12}$$

Eq. (5.12) presents a mapping between the Greens functions in chain space and the ones in band space.  $G_{\parallel}$  is the intra-chain propagator and  $G_{\perp}$  the inter-chain propagator, respectively.

## 5.2. Ladder with a magnetic field

We now want to include magnetic field in our model. The problem of a ladder in a magnetic field has been discussed in [9] (but without disorder), they show that large magnetic fields modify the band structure in a relevant way, even a gap can open. In order to use a linearized model we restrict ourselves to low magnetic fields.

We start directly with the linearized kinetic Hamiltonian:

$$H_{\text{kin}} = \int dx \left[ iv_f \sum_n \left( R_n^\dagger(x) \partial_x R_n(x) - L_n^\dagger(x) \partial_x L_n(x) \right) + t_\perp \left( R_1^\dagger R_2 + L_1^\dagger L_2 + h.c. \right) \right]. \quad (5.13)$$

R- and L-operators denote chirality, n denotes chain index. Note that disorder has already been neglected in this expression, disorder is introduced as before by inserting a lifetime to the resulting Greens functions.

Magnetic field is now included by the minimal substitution

$$\partial_x \rightarrow \partial_x + i \frac{e}{\hbar} A_x \quad (5.14)$$

and the Peierls substitution [31]

$$t_\perp \rightarrow t_\perp e^{-i \frac{e}{\hbar} \int \mathbf{A} dl}. \quad (5.15)$$

The Peierls substitution takes into account that an electron picks up some phase when hopping to another site. So the integral has to be performed on the way the electron takes on hopping, in our case, this is going from one chain to the other. The integral is therefore performed in y-direction from 0 to  $a_y$ , but one still has to care about the direction of hopping: hopping in the opposite direction leads to switching of the integral limits and therefore yields an additional minus sign.

Since the integral in (5.15) is performed in y-direction it only contains the y component of the vector potential  $\mathbf{A}$ , so  $A_x$  is accounted in (5.14),  $A_y$  in (5.15). However, due to gauge invariance we can choose the vector potential in a way that either  $A_x$  or  $A_y$  is zero, in this way we only have to perform one substitution.

We apply the magnetic field perpendicular to the chain and we choose the vector potential to be

$$\mathbf{A} = Bx \mathbf{e}_y, \quad (5.16)$$

which leads us to

$$t_\perp \rightarrow t_\perp \exp \left[ \mp i \frac{e}{\hbar} B x a_y \right] = t_\perp \exp \left[ \mp i 2\pi \frac{B}{\Phi_0} \frac{a_y}{2} x \right] = t_\perp \exp [\mp i 2\pi f x], \quad (5.17)$$

with the flux quantum  $\Phi_0 = h/2e$  and the ‘‘magnetic flux’’

$$f = \frac{B a_y}{2\Phi_0}. \quad (5.18)$$

Our definition of flux has the dimension  $[\text{length}^{-1}]$ , whereas flux in principle should be dimensionless. The reason is that we omitted  $a_x$  and are therefore left with only one length scale, namely  $a_y$ . Nevertheless we use the quantity  $f$  throughout the thesis just as a function of the magnetic field. The different signs in (5.17) denote hopping in different directions. With the Peierls substitution the hopping terms in the Hamiltonian can be rewritten

$$t_{\perp} e^{-i2\pi f x} R_1^{\dagger} R_2 = t_{\perp} \left( e^{i\pi f x} R_1 \right)^{\dagger} \left( e^{-i\pi f x} R_2 \right), \quad (5.19a)$$

$$t_{\perp} e^{i2\pi f x} R_2^{\dagger} R_1 = t_{\perp} \left( e^{-i\pi f x} R_2 \right)^{\dagger} \left( e^{i\pi f x} R_1 \right). \quad (5.19b)$$

We get analogous equations for the left-moving operators  $L_{1,2}$ . In order to get rid of the phase factors in the hopping term we perform a transformation

$$R_1 = e^{-i\pi f x} \tilde{R}_1, \quad R_2 = e^{i\pi f x} \tilde{R}_2, \quad (5.20a)$$

$$L_1 = e^{-i\pi f x} \tilde{L}_1, \quad L_2 = e^{i\pi f x} \tilde{L}_2. \quad (5.20b)$$

Now the Hamiltonian reads

$$\begin{aligned} H_{\text{kin}} = \int dx & \left[ i v_f \left( \tilde{R}_1^{\dagger}(x) \partial_x \tilde{R}_1(x) - i\pi f \tilde{R}_1^{\dagger}(x) \tilde{R}_1(x) - \tilde{L}_1^{\dagger}(x) \partial_x \tilde{L}_1(x) + i\pi f \tilde{L}_1^{\dagger}(x) \tilde{L}_1(x) \right. \right. \\ & + \tilde{R}_2^{\dagger}(x) \partial_x \tilde{R}_2(x) + i\pi f \tilde{R}_2^{\dagger}(x) \tilde{R}_2(x) - \tilde{L}_2^{\dagger}(x) \partial_x \tilde{L}_2(x) - i\pi f \tilde{L}_2^{\dagger}(x) \tilde{L}_2(x) \left. \right) \\ & + t_{\perp} \left( \tilde{R}_1^{\dagger}(x) \tilde{R}_2(x) + \tilde{L}_1^{\dagger}(x) \tilde{L}_2(x) + h.c. \right) \left. \right]. \quad (5.21) \end{aligned}$$

This result can also be achieved using the minimal substitution. The Hamiltonian reads in momentum space

$$\begin{aligned} H_{\text{kin}} = \int \frac{dk}{2\pi} & \left[ v_f \left( (k + \pi f) (R_1^{\dagger}(k) R_1(k) - L_1^{\dagger}(k) L_1(k)) \right. \right. \\ & + (k - \pi f) (R_2^{\dagger}(k) R_2(k) - L_2^{\dagger}(k) L_2(k)) \left. \right) \\ & + t_{\perp} \left( R_1^{\dagger}(k) R_2(k) + L_1^{\dagger}(k) L_2(k) + h.c. \right) \left. \right]. \quad (5.22) \end{aligned}$$

We now want to diagonalize this Hamiltonian. We start with an expression

$$R_1 = u_R R_+ + v_R R_-, \quad R_2 = v_R R_+ - u_R R_-, \quad (5.23)$$

and an analogous one for the left-movers. Note that the only difference between right- and left-movers is the sign of  $v_f$ . We find for the coherence factors  $u$  and  $v$

$$u_R^2 = \frac{1}{2} \left[ 1 + \frac{v\pi f}{\sqrt{(v\pi f)^2 + t_{\perp}^2}} \right] = \frac{1}{2} [1 + \alpha], \quad (5.24a)$$

$$v_R^2 = \frac{1}{2} \left[ 1 - \frac{v\pi f}{\sqrt{(v\pi f)^2 + t_{\perp}^2}} \right] = \frac{1}{2} [1 - \alpha], \quad (5.24b)$$

and for the left movers

$$u_L^2 = \frac{1}{2} [1 - \alpha], \quad v_L^2 = \frac{1}{2} [1 + \alpha], \quad (5.25)$$

where  $\alpha$  is given by

$$\alpha = \frac{v_f \pi f}{\sqrt{(v_f \pi f)^2 + t_\perp^2}} \in [0, 1]. \quad (5.26)$$

This diagonalization leads to the dispersions

$$\epsilon_\pm^R(k) = v_f k \pm \sqrt{(v_f \pi f)^2 + t_\perp^2}, \quad (5.27a)$$

$$\epsilon_\pm^L(k) = -v_f k \pm \sqrt{(v_f \pi f)^2 + t_\perp^2}. \quad (5.27b)$$

Obviously, the band splitting is influenced by magnetic field. This splitting can also be found in  $\Delta k$

$$\Delta k = \frac{2}{v_f} \sqrt{(v_f \pi f)^2 + t_\perp^2}, \quad (5.28)$$

so magnetic field enhances the splitting of the two bands. Fig. 5.4 shows again a plot of the linearized spectrum where  $\Delta k$  is inserted. The retarded Greens-function in band space is then given by

$$G_\pm^{R/L}(\omega, k) = \frac{1}{\omega - \epsilon_\pm^{R/L}(k) + i/2\tau}. \quad (5.29)$$

Disorder has been taken into account by a finite relaxation time  $\tau$ , in analogy to the former section. The Greens functions in chain space are given by

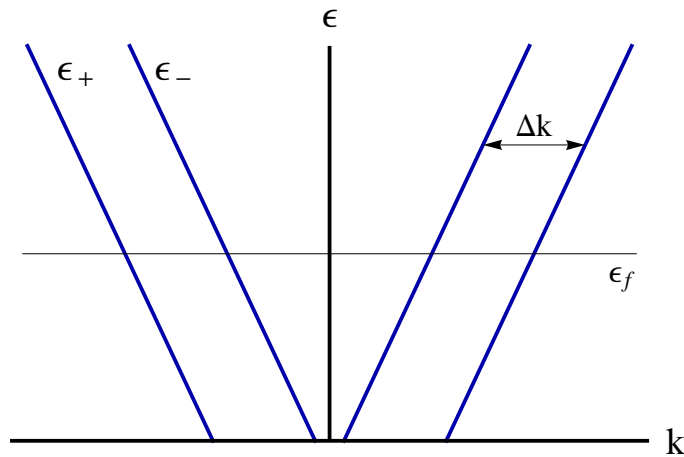


Figure 5.4.: Linearized band spectrum.  $\Delta k$  is shown in this plot for the sake of clarity.

$$G_{1,1}^R = \frac{1}{2} (G_+^R + G_-^R) - \frac{1}{2} \alpha (G_+^R - G_-^R), \quad (5.30a)$$

$$G_{2,2}^R = \frac{1}{2} (G_+^R + G_-^R) + \frac{1}{2} \alpha (G_+^R - G_-^R), \quad (5.30b)$$

$$G_{1,2}^R = G_{2,1}^R = \frac{1}{2} \sqrt{1 - \alpha^2} (G_+^R - G_-^R) \quad (5.30c)$$

and

$$G_{1,1}^L = \frac{1}{2} (G_+^L + G_-^L) + \frac{1}{2} \alpha (G_+^L - G_-^L), \quad (5.31a)$$

$$G_{2,2}^L = \frac{1}{2} (G_+^L + G_-^L) - \frac{1}{2} \alpha (G_+^L - G_-^L), \quad (5.31b)$$

$$G_{1,2}^L = G_{2,1}^L = \frac{1}{2} \sqrt{1 - \alpha^2} (G_+^L - G_-^L). \quad (5.31c)$$

Note that the magnetic field has broken the symmetry between the two chains. The intra-chain propagators became different, depending on the chain and the chirality. As shown in fig. 5.5, magnetic field forces the electrons to perform loops around the plaquettes. Consequently, electrons on chain 1 collect a different phase than the electrons on chain 2 and the symmetry is broken.

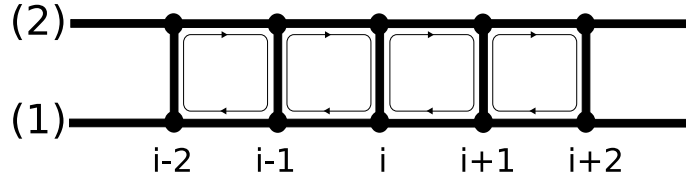


Figure 5.5.: Ladder in a magnetic field. Magnetic field forces the electrons to perform loops, therefore the electrons on different chains acquire different phases.

## 6. Weak Localization in the 2-chain ladder

We now want to turn to the main problem, the magnetoresistance induced by weak localization. The weak localization correction for a single chain has been calculated by [19, 37], which inspired this work.

The underlying ladder model has been discussed in the last chapter, including disorder and e-e interaction. As already noted in sec. 3.2 and 4.2, e-e interaction scatters only forwards whereas disorder scatters only backwards in our model. Disorder has already been treated in the last chapter and is accounted via a relaxation time  $\tau$ , but what is still missing is a treatment of the electron-electron interaction. e-e interaction leads to two relevant effects. First of all, impurity scattering becomes renormalized [17, 30] and leads to a renormalized relaxation time  $\tau \rightarrow \tilde{\tau}$ . We have not looked at this effect in detail and assumed that we use the renormalized  $\tilde{\tau}$  throughout the whole thesis.

The second effect of e-e interaction is dephasing. This mechanism has been explained in sec. 2.3 and serves as a cutoff for the weak localization correction. We restrict ourselves to the case of strong dephasing ( $\tau_\phi/\tau \ll 1$ ), which is valid for sufficiently high temperatures and low enough disorder densities. In this case we only have to retain the shortest possible Cooperon, which is the one with two impurities. Such a process is presented in fig. 6.1, including the according physical processes in real space. It can be seen that the A-process cannot scatter on both impurities, since we include only backscattering off impurities. Thus, diagrams containing two impurities yield zero.

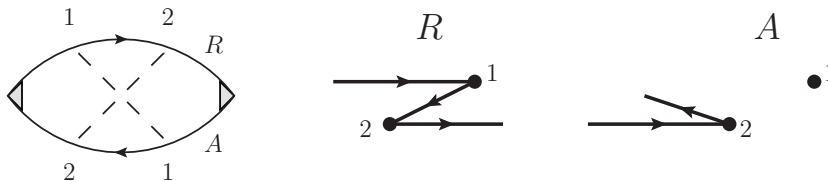


Figure 6.1.: 2-impurity Cooperon with the according physical processes in real space. The R process can scatter on both impurities, whereas the A process scatters only on one impurity. Scattering on the second one is not possible because we include only backscattering off impurities.

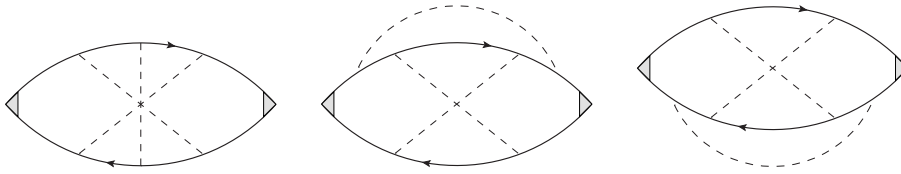


Figure 6.2.: WL-diagrams with 3 impurities. Solid lines are electron Greens-functions (already dressed by e-e-interactions), dashed lines denote backscattering off impurities.

So the leading order contributions to the weak localization are the diagrams with 3 impurities, which are shown in fig. (6.2). We will focus our calculation here on the fully crossed diagram, it will turn out the the other ones yield the same result.

In order to get magnetoresistance, one has to enclose a finite space when the electron gets scattered off the impurities. One possible process is presented in fig. 6.3. Of course this is not the only possible setup for the impurities, others can also yield magnetoresistance. In order to symmetrize the problem, we sum over all possible setups.

The remaining question is how to tackle e-e interaction, this is done using two approaches.

- **phenomenological approach**

In this approach we do not care about the exact structure of the interaction. We already discussed the effects of e-e interaction and take it into account via a phenomenological dephasing time  $\tau_\phi$ . This technique is very qualitatively, but in the end it yields an analytical result.

- **microscopic approach**

The second approach takes interaction into account in a proper way using Functional Bosonization. This approach is quantitative, in contrast to the first one, but leads to a complicated integral.

After calculating the correction, both approaches are compared in the very end for two reasons: First of all, the validity of the phenomenological model has to be checked and second, we want a connection of the phenomenological dephasing time  $\tau_\phi$  to system-inherent quantities.

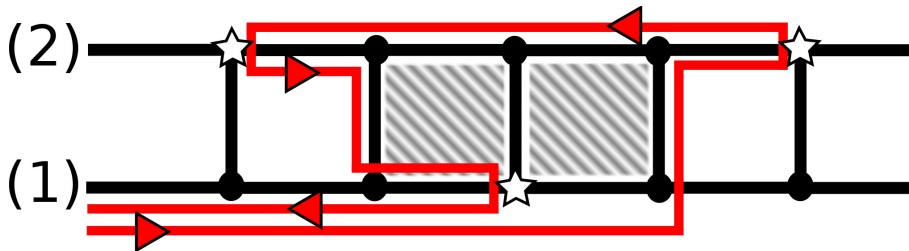


Figure 6.3.: Example of a possible impurity setup. The path connecting all 3 impurities encloses a finite area, which is drawn shaded.

## 6.1. Phenomenological approach

In this section we want to calculate the conductivity correction of the 3-impurity diagrams. The diagram we are going to calculate is given in fig. 6.4. Note that this is a current bubble and the vertices are dressed by a factor of  $ev_f$ . In addition, the Diffuson correction has been included, denoted by triangles attached to the vertices.

We use the Greens functions (5.29), but we have to modify them. As mentioned in sec. 2.2, low-angle scattering doesn't affect the conductivity, so we take only backscattering off impurities into account. Consequently, the disorder-induced relaxation time  $\tau_q$  (given by eq. (2.6)) has to be modified and becomes replaced by  $\tau = \tau_q/2$ . Now the retarded Greens function reads

$$G_{\pm}^{R/L}(\omega, k) = \frac{1}{\omega - \epsilon_{\pm}^{R/L}(k) + i/2\tau_q} = \frac{1}{\omega - \epsilon_{\pm}^{R/L}(k) + i/4\tau} \quad (6.1)$$

Since each current vertex is renormalized by the Diffuson (see section 2), we have to add a factor of  $\tau/\tau_q$  to each of them. The correction for the fully crossed diagram reads

$$\text{Diagram} = \sigma_{C3} = -2 \left( \frac{\tau}{\tau_q} ev_f \right)^2 D_{C3}. \quad (6.2)$$

The factor  $\tau ev_f/\tau_q$  comes from the 2 current vertices, the factor 2 represents the two choices we have to choose chirality and the Kernel  $D_{C3}$  is given by

$$D_{C3} = \frac{1}{(2\pi\rho\tau)^3} \sum_{ijklm=1,2} \int \frac{d\epsilon}{2\pi} \left( -\frac{\partial f_{\epsilon}}{\partial \epsilon} \right) \int \frac{dp}{2\pi} \frac{dp_1}{2\pi} \frac{dp_2}{2\pi} \frac{dQ}{2\pi} \\ G_{i,j}^R(p) G_{j,k}^L(p_1) G_{k,l}^R(p_2) G_{l,m}^L(-p+Q) \times \\ \times [G_{i,l}^R(p) G_{l,k}^L(-p_2+Q) G_{k,j}^R(-p_1+Q) G_{j,m}^L(-p+Q)]^*. \quad (6.3)$$

The sum stands for the different chain setups, the  $\epsilon$ -integration comes from summation over Matsubara frequencies (this can be looked up in detail in Appendix B). It turns out

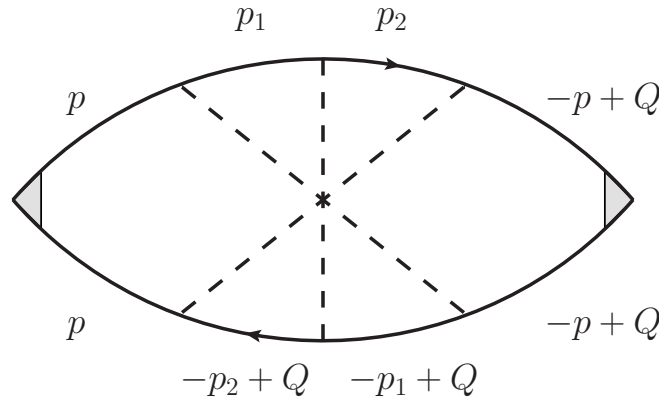


Figure 6.4.: Feynman diagram of the fully crossed 3-impurity Cooperon with corresponding momenta.

that the integrand is energy-independent, so we only have to integrate over the derivative of the Fermi-function. The factor  $(2\pi\rho\tau)^{-1}$  comes from averaging over the scattering potential ( $\rho$  is the density of states at the Fermi point)

$$\frac{1}{L} \langle |U(k)|^2 \rangle = \frac{1}{2\pi\rho\tau}, \quad (6.4)$$

and the Greens functions in chain space are given by (5.30) and (5.31).

The calculation of the integral is done using Mathematica, because the expression gets very big if one inserts the Greens functions in chain basis and sums over all possible chain setups. For this purpose we introduced an All-In-One Greens function

$$G_{a,b}^{R/L} = \frac{1}{2} \sqrt{1 - \frac{1 - (-1)^{a+b}}{2} \alpha^2} \left( G_+^{R/L} + (-1)^{a+b} G_-^{R/L} \right) \pm \frac{(-1)^a + (-1)^b}{2} \frac{\alpha}{2} \left( G_+^{R/L} - G_-^{R/L} \right). \quad (6.5)$$

Since the calculation is done in Mathematica we present only the cornerstones and some important results. First we notice that the  $p_i$ -integrations in 6.3 factorize, so it is straightforward to start with these. We start with the Greens functions connected to the current vertices. All of them contain momentum  $p$  and can be expanded using partial fraction decomposition:

$$G_{\pm}^{R/L}(p)(G_{\pm}^{R/L}(p))^* = 2i\tau(G_{\pm}^{R/L}(p) - (G_{\pm}^{R/L}(p))^*), \quad (6.6a)$$

$$G_+^{R/L}(p)(G_-^{R/L}(p))^* = iC(G_+^{R/L}(p) - (G_-^{R/L}(p))^*), \quad (6.6b)$$

$$G_-^{R/L}(p)(G_+^{R/L}(p))^* = iC^*(G_-^{R/L}(p) - (G_+^{R/L}(p))^*), \quad (6.6c)$$

with the factor

$$C = \left( \frac{1}{2\tau} + i\Delta\epsilon \right)^{-1}. \quad (6.7)$$

Equations (6.6) reduce the  $p$ -integrand from a product of 4 Greens functions to a sum over products of 2 Greens functions. The only remaining integrals are all of the same form:

$$F_{ij}^{pq}(Q) = \frac{1}{2\pi\rho\tau} \int \frac{dp}{2\pi} G_i^p(p) G_j^{q*}(Q-p) = F_{ji}^{qp}(Q)^*. \quad (6.8)$$

Remember that upper indices denote chirality (R/L) whereas lower ones denote band index (+/-). So in the end we are left with the  $Q$ -integration over a product of 3 F-functions. Of course, we have to sum up all the different combinations of F-functions we get from summing over the chain setups.

In order to compute the F-functions, we use the Greens functions in band space (6.1), but we insert a phenomenological dephasing time  $\tau_\phi \ll \tau$

$$G_{\pm}^{R/L}(\omega, k) \rightarrow \frac{1}{\omega - \epsilon_{\pm}^{R/L}(k) + i/4\tau + i/2\tau_{\phi}}$$

$$\xrightarrow{\tau_{\phi} \ll \tau} \frac{1}{\omega - \epsilon_{\pm}^{R/L}(k) + i/2\tau_{\phi}}. \quad (6.9)$$

Note that the effect of dephasing is only important for the effect of weak localization, that is, when two paths interfere coherently (see 2.3 for details). Having said this, dephasing has to be included only in the Greens functions describing the loop, which are the ones depicted in fig. 6.4. The Greens functions in the Diffuson correction do not get this extra  $\tau_{\phi}$ , since the effect of dephasing has no effect here.

We can now compute the F-functions and get

$$F_{++}^{LR}(Q) = F_{--}^{LR}(Q) = \frac{1}{2\tau} \frac{1}{1/\tau_{\phi} + iv_f Q}, \quad (6.10a)$$

$$F_{+-}^{LR}(Q) = \frac{1}{2\tau} \frac{1}{1/\tau_{\phi} + iv_f(Q - \Delta k)}, \quad (6.10b)$$

$$F_{-+}^{LR}(Q) = \frac{1}{2\tau} \frac{1}{1/\tau_{\phi} + iv_f(Q + \Delta k)}, \quad (6.10c)$$

where we used  $\rho = (\pi v_f)^{-1}$ . One immediately sees that the F-functions contain only single poles, so the Q-Integration is just a simple residual integral.

The calculation has so far only governed the fully crossed 3-impurity diagram. As shown in Fig. 6.4, one has to include 2 other diagrams. The calculation of these diagrams is very similar to the calculation of the fully crossed diagram and it turns out that the two diagrams on the right of Fig. 6.4 yield the same result as the fully crossed diagram, so

$$\text{Diagram 1} + \text{Diagram 2} + \text{Diagram 3} = \sigma_{WL} = 2\sigma_{C3} \quad (6.11)$$

One can also check that Drude conductivity is not influenced by our model because we have only one Fermi velocity, so there's still

$$\sigma_D = \frac{e^2 v_f \tau}{\pi}. \quad (6.12)$$

We have now prepared everything, and after evaluating the Q-integration and summing over all chains we get

$$\sigma_{WL} = -\frac{1}{8}\sigma_D \left(\frac{\tau_{\phi}}{\tau}\right)^2 K_{phen}(\alpha, v_f \tau_{\phi} \Delta k). \quad (6.13)$$

$K_{phen}$  is given by

$$\begin{aligned}
K_{phen}(\alpha, v_f \tau_\phi \Delta k) = \frac{1}{4} & \left[ \alpha^0 \left( 5 + \frac{1}{1 + (v_f \tau_\phi \Delta k)^2} + \frac{2}{(1 + (v_f \tau_\phi \Delta k)^2)^2} \right) \right. \\
& + \alpha^2 \left( -9 + \frac{-9}{1 + (v_f \tau_\phi \Delta k)^2} + \frac{-2}{(1 + (v_f \tau_\phi \Delta k)^2)^2} \right. \\
& \quad \left. + \frac{32}{4 + (v_f \tau_\phi \Delta k)^2} + \frac{192}{(4 + (v_f \tau_\phi \Delta k)^2)^2} \right) \\
& + \alpha^4 \left( 15 + \frac{15}{1 + (v_f \tau_\phi \Delta k)^2} + \frac{-2}{(1 + (v_f \tau_\phi \Delta k)^2)^2} \right. \\
& \quad \left. + \frac{-48}{4 + (v_f \tau_\phi \Delta k)^2} + \frac{-256}{(4 + (v_f \tau_\phi \Delta k)^2)^2} \right) \\
& + \alpha^6 \left( -3 + \frac{-7}{1 + (v_f \tau_\phi \Delta k)^2} + \frac{2}{(1 + (v_f \tau_\phi \Delta k)^2)^2} \right. \\
& \quad \left. + \frac{16}{4 + (v_f \tau_\phi \Delta k)^2} + \frac{64}{(4 + (v_f \tau_\phi \Delta k)^2)^2} \right) \left. \right], \quad (6.14)
\end{aligned}$$

with

$$\alpha = \frac{v \pi f}{\sqrt{(v \pi f)^2 + t_\perp^2}} \in [0, 1] \quad (6.15)$$

and

$$\Delta k = \frac{2}{v_f} \sqrt{(v_f \pi f)^2 + t_\perp^2}. \quad (6.16)$$

This result looks very complicated at first glance, but  $K_{phen}$  nevertheless exhibits some specific structure. The most obvious feature is the appearance of different powers of  $\alpha$ . Note that the formula is exact, although it looks like a power series expansion in  $\alpha$ . The highest power of  $\alpha$  is determined by the number of impurities in the Cooperon. Every factor of  $\alpha$  is multiplied by a prefactor which contains even more functions. These prefactors exhibit also a very special structure, as they consist of just a few functions, but each with a different prefactor.

## 6.2. Microscopic approach

In the last section we derived a weak localization correction using disordered Greens functions and inserting a phenomenological dephasing time. This led us to an analytical result which we can study easily, but we still do not know how reasonable this approach is. In this section we want to use the Functional Bosonization technique explained in section 4. Using this approach, we include electron-electron interaction (which leads to dephasing) properly, therefore we are able to check if the simple approach is correct.

Let us briefly recatch the results obtained in sec. 4. The full Greens function can be written as a product of the free Greens function with a phase factor,

$$G^R(x, \tau) = g^R(x, \tau) \exp[-B_{RR}(x, \tau)]. \quad (6.17)$$

Interaction is included in the  $B_{\mu\nu}$ -correlators, these are given in Appendix C. Impurity vertices lead to factors of

$$Q(x, \tau) = \exp [B_{RR}(x, \tau) + B_{LL}(x, \tau) - 2B_{RL}(x, \tau)] \quad (6.18)$$

and  $Q^{-1}(x, \tau)$ . Each pair of impurity vertices at  $(x_N, \tau_N)$  and  $(x_{N'}, \tau_{N'})$  leads to a factor of  $Q(x_N - x_{N'}, \tau_N - \tau_{N'})$  if the incident chiralities are the same and to a factor of  $Q^{-1}(x_N - x_{N'}, \tau_N - \tau_{N'})$  if they are different. Every pair of impurity vertices has to be accounted by such a factor.

Since the derivation of the Functional Bosonization in section 4 is done for purely one dimensional systems we have to check how the 2 chain model affects this results. The 2 chain model yields two bands with different Fermi points  $k_{f,\pm}$ , so we can calculate the free Greens function in band space:

$$\begin{aligned} g_{\pm}^R(x, \tau) &= T \sum_{\Omega} e^{-i\Omega\tau} \int \frac{dq}{2\pi} \frac{e^{iqx}}{v_f(q - k_{f,\pm}) - i\Omega} \\ &= T \sum_{\Omega} e^{-i\Omega\tau} \int \frac{dq}{2\pi} \frac{e^{i(q+k_{f,\pm})x}}{v_f q - i\Omega} \\ &= e^{ik_{f,\pm}x} T \sum_{\Omega} e^{-i\Omega\tau} \int \frac{dq}{2\pi} \frac{e^{iqx}}{v_f q - i\Omega} \\ &= e^{ik_{f,\pm}x} g_0^R(x, \tau), \end{aligned} \quad (6.19)$$

and in analogy

$$g_{\pm}^L(x, \tau) = e^{-ik_{f,\pm}x} g_0^L(x, \tau). \quad (6.20)$$

Note that free Greens functions in the 2 chain model reduce to the simple Greens functions  $g_0^{R/L}(x, \tau)$  given by (4.14) and a phase factor which contains the band property (namely, the Fermi point  $k_{f,\pm}$ ). The  $B_{\mu,\nu}$ -correlators (see equation (4.19)) aren't affected by the shift of the Fermi points because they are bosonic correlators and only couple densities. The only way the Fermi points could appear in this correlator is upon backscattering, but as already discussed we neglect backscattering in the interaction.

As before, one starts the calculation in real space and has to perform a transformation into band space. The transformation is given by eq. (5.30) and (5.31), inserting eq. (6.19) into the transformation rules gives

$$\begin{aligned} g_{1,1}^R &= \frac{1}{2} (g_+^R + g_-^R) - \frac{1}{2} \alpha (g_+^R - g_-^R) \\ &= \left\{ \frac{1}{2} (e^{ik_{f,+x}} + e^{ik_{f,-x}}) - \frac{1}{2} \alpha (e^{ik_{f,+x}} - e^{ik_{f,-x}}) \right\} g_0^R, \end{aligned} \quad (6.21)$$

for example. Note that the free Greens functions and the phase factors separate completely, this holds for any transformation given in eq. (5.30) and (5.31).

The calculation of the weak localization correction for one 1D chain has been performed in [37] and is quite complicated. We want to adopt this calculation for our model of 2 chains or 2 bands, respectively. The interested reader might consider the original paper for technical details of the calculation.

We consider only forward scattering in the interaction, so in terms of the *g-ology* model (explained in sec. 3.2) we include only the  $g_2$  and  $g_4$  processes. Hence, the interaction Hamiltonian (5.2c) reads

$$H_{\text{int}} = \frac{1}{2} \sum_{\mu s s'} \int dx (n_{\mu s} g_4 n_{\mu s'} + n_{\mu s} g_2 n_{-\mu s'}), \quad (6.22)$$

with the densities  $n_{\mu,s}$ , chirality  $\mu = R/L$  and band index  $s = \pm$ . Since both interaction processes relate to the  $V(q = 0)$  matrix element, we set  $g_2 = g_4 = g$ . The two bands introduce two types of species to our model, the band index  $s$  thus serves as a pseudospin. Consequently, we use the spinful  $B_{\mu\nu}$ -correlators given in Appendix C.

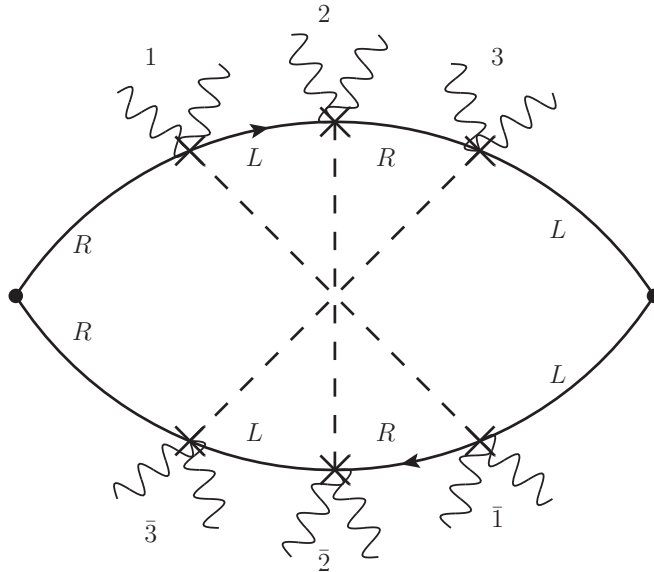


Figure 6.5.: Cooperon in the functional bosonization approach. The solid lines are free electron Greens functions, the dashed line is an impurity scattering line and the wavy lines are phase factors due to electron-electron interaction.

The weak localization correction is still given by the Cooperon with 3 impurities, electron-electron interaction is included via the phase factors attached to the impurity scattering vertices, which leads to the diagram presented in fig. 6.5.

As discussed in section 4.2, averaging leads us to a bunch of  $Q(x, \tau)$ - and  $Q^{-1}(x, \tau)$ -functions which contain the interaction. The weak localization correction reads after averaging over the  $\Theta$ -field:

$$\begin{aligned}
\sigma_{WL}(i\Omega_m) &= 4(ev_f)^2 \left( \frac{v_f^2}{2l_0} \right)^3 \frac{1}{\Omega_m} \frac{T}{L} \sum_{ijklm} \int_0^{1/T} d\tau_1 d\bar{\tau}_1 d\tau_2 d\bar{\tau}_2 d\tau_3 d\bar{\tau}_3 \int dx_1 dx_2 dx_3 \\
&\times [g_0^R(x_1 - x_3, \tau_1 - \bar{\tau}_3) Q^{-1}(x_1 - x_3, \tau_1 - \bar{\tau}_3)] [g_{j,k}^L(x_2 - x_1, \tau_2 - \tau_1) Q^{-1}(x_2 - x_1, \tau_2 - \tau_1)] \\
&\times [g_{k,l}^R(x_3 - x_2, \tau_3 - \bar{\tau}_2) Q^{-1}(x_3 - x_2, \tau_3 - \bar{\tau}_2)] [g_0^L(x_1 - x_3, \bar{\tau}_1 - \tau_3) Q^{-1}(x_1 - x_3, \bar{\tau}_1 - \tau_3)] \\
&\times [g_{j,k}^R(x_2 - x_1, \bar{\tau}_2 - \bar{\tau}_1) Q^{-1}(x_2 - x_1, \bar{\tau}_2 - \bar{\tau}_1)] [g_{i,j}^L(x_3 - x_2, \bar{\tau}_3 - \bar{\tau}_2) Q^{-1}(x_3 - x_2, \bar{\tau}_3 - \bar{\tau}_2)] \\
&\times Q(x_1 - x_3, \tau_1 - \tau_3) Q(x_1 - x_3, \bar{\tau}_1 - \bar{\tau}_3) Q(x_1 - x_2, \tau_1 - \bar{\tau}_2) Q(x_2 - x_1, \tau_2 - \bar{\tau}_1) \\
&\times Q(x_3 - x_2, \tau_3 - \bar{\tau}_2) Q(x_2 - x_3, \tau_2 - \bar{\tau}_3) Q^{-1}(0, \tau_1 - \bar{\tau}_1) Q^{-1}(0, \tau_2 - \bar{\tau}_2) \\
&\times Q^{-1}(0, \tau_3 - \bar{\tau}_3) \mathcal{W}_{i,j,l}^{in,R}(x_1 - x_3, \tau_1, \bar{\tau}_3, \Omega_m) \mathcal{W}_{j,l,m}^{out,L}(x_1 - x_3, \bar{\tau}_1, \tau_3, \Omega_m). \tag{6.23}
\end{aligned}$$

One can easily check the averaging by comparing the  $Q(x, \tau)$ -functions in eq. (6.23) with fig. 6.5. The prefactor  $4 = 2 \cdot 2$  stems from the two choices of chirality and the two diagrams left (see fig. 6.2). The sum is over all possible chain setups, the factor  $(ev_f)$  stems from the the two current vertices and the factor of  $v_f^2/2l_0$  comes from the disorder potential

$$\frac{1}{L} \langle |U_b(k)|^2 \rangle = \frac{1}{2\pi\tau} \frac{1}{\rho} = \frac{v_f}{2\pi l_0} \pi v_f = \frac{v_f^2}{2l_0}, \tag{6.24}$$

where we used  $\rho = (\pi v_f)^{-1}$ . The  $\mathcal{W}$  factors stem from integration over the two Greens functions attached to the current vertices over the external coordinates and times:

$$\begin{aligned}
&\int dx_i d\tau_i e^{-i\Omega_m \tau_i} g_{r,s}^{R/L}(x_1 - x_i, \tau_1 - \tau_i) g_{r,t}^{R/L}(x_i - x_3, \tau_i - \bar{\tau}_3) \\
&= g_0^{R/L}(x_1 - x_3, \tau_1 - \bar{\tau}_3) \mathcal{W}_{r,s,t}^{in,R/L}(x_1 - x_3, \tau_1, \bar{\tau}_3, \Omega_m). \tag{6.25}
\end{aligned}$$

The  $\mathcal{W}$  functions have been calculated in Appendix A, but only in band space. This means that we inserted equation (6.5) in equation (6.25) and calculated the integral which yields

$$\begin{aligned}
\mathcal{W}_{i,j}^{in,R}(x, \tau_\alpha, \tau_\beta, \Omega_m) &= \\
&= -i \frac{\text{sgn}(\Omega_m)}{|\Omega_m| + 2v_f/l + i\text{sgn}(\Omega_m)v_f\Delta k} \left( e^{-i\Omega_m\tau_\alpha} e^{ik_{f,j}x} - e^{-i\Omega_m\tau_\beta} e^{ik_{f,i}x} \right), \tag{6.26}
\end{aligned}$$

where  $i, j = \pm$  are band indices and  $\Delta k = k_{f,j} - k_{f,i}$ . The  $\mathcal{W}$  functions fulfill the relations

$$\begin{aligned}
\mathcal{W}^{in/f,R}(x, \tau_\alpha, \tau_\beta, \Omega_m) &= -\mathcal{W}^{in/f,L}(-x, \tau_\alpha, \tau_\beta, \Omega_m), \\
\mathcal{W}^{in,R/L}(x, \tau_\alpha, \tau_\beta, \Omega_m) &= \mathcal{W}^{out,R/L}(x, \tau_\alpha, \tau_\beta, -\Omega_m). \tag{6.27}
\end{aligned}$$

Since we include only backscattering off disorder we have to replace the scattering rate  $2v_f/l = 2/\tau$  in the vertices by  $v_f/l$ , in analogy to the Diffuson correction on the phenomenological model. We introduce a new set of variables:

$$\begin{aligned}
x_a &= x_1 - x_3, \\
x_b &= x_3 - x_2, \\
x_c &= x_1 - x_2, \\
\tau_a &= \tau_1 - \bar{\tau}_3, \\
\tau_b &= \tau_3 - \tau_2, \\
\tau_c &= \tau_2 - \tau_1, \\
\bar{\tau}_a &= \bar{\tau}_1 - \tau_3, \\
\bar{\tau}_b &= \bar{\tau}_3 - \bar{\tau}_2, \\
\bar{\tau}_c &= \bar{\tau}_2 - \bar{\tau}_1.
\end{aligned} \tag{6.28}$$

The next steps are the same as in [37] and can be looked up in the paper in detail. Note that the only thing new to these formulas are the phase factors containing the different Fermi points and a sum over different chains. These phase factors are the only functions which are connected to the summation indices, so the summation is completely decoupled from the Greens functions and the  $Q$ -correlators

After summing over all chains and performing the same steps as in [37] we find

$$\begin{aligned}
\frac{\sigma_{WL}}{\sigma_D} &= \lim_{\Omega \rightarrow 0} \left\{ -\frac{2\pi T}{\Omega_m} \frac{v^4}{32l^4} \frac{v^4}{(|\Omega_m| + v/l)^2} \sum_n \int_0^\infty dx_a dx_b dx_c \delta(x_a + x_b - x_c) \right. \\
&\quad \times G_+^r(x_a, i\epsilon_n + i\Omega_m) G_+^r(x_b, i\epsilon_n + i\Omega_m) G_+^r(x_c, i\epsilon_n + i\Omega_m) \\
&\quad \left. \times G_+^a(x_a, i\epsilon_n) G_+^a(x_b, i\epsilon_n) G_+^a(x_c, i\epsilon_n) A_{WL}(\alpha, \Delta k x_a, \Delta k x_b, \Delta k x_c) \right\}_{i\Omega_m \rightarrow \Omega + i0},
\end{aligned} \tag{6.29}$$

where the space-energy Greens functions are given in Appendix C. The Kernel  $A_{WL}$  is given by

$$\begin{aligned}
A_{WL}(\alpha, x_a, x_b, x_c) &= \frac{1}{4} \left\{ \alpha^0 [5 + \cos(2x_a) + \cos(2x_b) + \cos(2x_c)] \right. \\
&\quad + \alpha^2 [-9 + 6(\cos(x_a) + \cos(x_b) + \cos(x_c)) \\
&\quad \quad - 1(\cos(2x_a) + \cos(2x_b) + \cos(2x_c)) \\
&\quad \quad - 2(\cos(x_a - x_b) + \cos(x_a + x_c) + \cos(x_b + x_c))] \\
&\quad + \alpha^4 [15 - 8(\cos(x_a) + \cos(x_b) + \cos(x_c)) \\
&\quad \quad - 1(\cos(2x_a) + \cos(2x_b) + \cos(2x_c)) \\
&\quad \quad + 4(\cos(x_a - x_b) + \cos(x_a + x_c) + \cos(x_b + x_c))] \\
&\quad + \alpha^6 [-3 + (\cos(2x_a) + \cos(2x_b) + \cos(2x_c)) \\
&\quad \quad + 2(\cos(x_c - x_a) + \cos(x_a + x_b) + \cos(x_c - x_b)) \\
&\quad \quad \left. - 2(\cos(x_a - x_b) + \cos(x_a + x_c) + \cos(x_b + x_c))] \right\}, \tag{6.30}
\end{aligned}$$

with

$$\alpha = \frac{v\pi f}{\sqrt{(v\pi f)^2 + t_{\perp}^2}} \in [0, 1] \quad (6.31)$$

and

$$\Delta k = \frac{2}{v_f} \sqrt{(v_f \pi f)^2 + t_{\perp}^2}. \quad (6.32)$$

After inserting the Greens functions, summing over the Matsubara frequencies, performing the analytical continuation  $i\Omega_m \rightarrow \Omega + i0$  and going to the DC limit  $\Omega \rightarrow 0$  we find for the weak localization correction

$$\sigma_{WL} = -\frac{1}{8}\sigma_D \left(\frac{l_{ee}}{l}\right)^2 K_{micro} \left(\alpha, \frac{\Delta k l_{ee}}{2}\right), \quad (6.33)$$

with the relaxation length  $l = v_f \tau$  and the electron-electron scattering length  $l_{ee} \simeq v_f^2/gT$  ( $g$  is the interaction strength,  $T$  is the temperature). The function  $K_{micro}$  is given by

$$K_{micro}(\alpha, \gamma) = \frac{\pi}{4} \int_{-\infty}^{\infty} \frac{dz}{\cosh^2(\pi z)} \int_0^{\infty} dx \int_0^{\infty} dy \times \quad (6.34)$$

$$\times \mathcal{R}(x, z) \mathcal{R}(y, z) \mathcal{R}(x + y + xy, z) A_{WL}(\alpha, \gamma x, \gamma y, \gamma(x + y)),$$

with

$$\mathcal{R}(x, z) = {}_2F_1(1/2 + iz, 1/2, 1; -x) {}_2F_1(1/2 - iz, 1/2, 1; -x), \quad (6.35)$$

where  ${}_2F_1$  is the Gauss hypergeometric function.

In order to get the actual correction we have to choose a specific value of  $\Delta k l_{ee}$  and evaluate the integral in eq. (6.34). Note that the function  $K_{micro}$  has a similar form as  $K_{phen}$  (given in eq. (6.14)).  $K_{micro}$  exhibits the same powers of  $\alpha$  times a prefactor. In addition, the structure of the prefactors also shows recurring functions, as seen in the phenomenological model.

### 6.3. Comparison of the two approaches

In the last two sections we have calculated the weak localization correction of the 2-chain ladder twice, using a phenomenological and a microscopic approach. In the phenomenological approach we have guessed the effect of e-e interaction and introduced a phenomenological dephasing time  $\tau_\phi$ . Since we do not know how good our guess was, we calculated the correction in a microscopic approach again using Functional Bosonization. Using this method we included interaction properly, it is taken into account via the electron-electron scattering length  $l_{ee} \simeq v_f^2/gT$  ( $g$  is interaction strength,  $T$  is temperature).

In this section we want to prove the validity of the first (phenomenological) approach by comparing it with the second (microscopic) one. We also want to find a relation between the length scales of the two approaches,  $v_f\tau_\phi$  and  $l_{ee}$ .

The two approaches led to

$$\sigma_{WL}^{phen} = -\frac{1}{8}\sigma_D \left(\frac{\tau_\phi}{\tau}\right)^2 K_{phen}(\alpha, v_f\tau_\phi\Delta k) \quad (6.36)$$

and

$$\sigma_{WL}^{micro} = -\frac{1}{8}\sigma_D \left(\frac{l_{ee}}{l}\right)^2 K_{micro}\left(\alpha, \frac{\Delta kl_{ee}}{2}\right). \quad (6.37)$$

On first glance, both results look pretty similar, they are both proportional to the Drude conductivity and to some ratio of  $\tau_\phi/\tau$  or  $l_{ee}/l$ , respectively. The remaining functions are given in eq. (6.14) ( $K_{phen}$ ) and 6.34 ( $K_{micro}$ ). Both functions exhibit a special structure in  $\alpha$ :

$$K = \alpha^0 p_0 + \alpha^2 p_2 + \alpha^4 p_4 + \alpha^6 p_6. \quad (6.38)$$

The  $p_i$ -functions, however, are different in the two approaches. In the phenomenological model it holds  $p_i = p_i(v_f\Delta k\tau_\phi)$ , whereas in the microscopic model  $p_i = p_i(\Delta kl_{ee}/2)$ . Moreover, the  $p_i$  are given by a complicated integral in the microscopic model.

Both approaches represent the same quantity, so

$$\begin{aligned} \sigma_{WL}^{phen} &= \sigma_{WL}^{micro} \\ \Rightarrow (v_f\tau_\phi)^2 K_{phen}(\alpha, v_f\tau_\phi\Delta k) &= l_{ee}^2 K_{micro}\left(\alpha, \frac{\Delta kl_{ee}}{2}\right) \end{aligned} \quad (6.39)$$

holds.  $\tau_\phi$  and  $l_{ee}$  appear in two ways in this formula, as an overall prefactor and as an argument of the function  $K$ . Since these two appearances have different origins, we treat them both separately and call the  $\tau_\phi$  in the prefactor  $\tilde{\tau}_\phi$ :

$$(v_f\tilde{\tau}_\phi)^2 K_{phen}(\alpha, v_f\tau_\phi\Delta k) = l_{ee}^2 K_{micro}\left(\alpha, \frac{\Delta kl_{ee}}{2}\right). \quad (6.40)$$

$\tilde{\tau}_\phi$  is determined easily, we choose  $\Delta k = 0$  and find

$$(v_f\tilde{\tau}_\phi)^2 \cdot 2 \simeq l_{ee}^2 \cdot 2.288 \quad \Rightarrow \quad v_f\tilde{\tau}_\phi \simeq 1.069l_{ee}. \quad (6.41)$$

To find a mapping of  $\tau_\phi$ , we calculate  $p_i^{micro}$  for different values of  $\Delta k l_{ee}/2$  and fit it with  $p_i^{phen}$ . The fit parameter is determined by

$$p_i^{phen}(v_f \Delta k \tau_\phi) = p_i^{phen} \left( \underbrace{\frac{2v_f \tau_\phi}{l_{ee}}}_{\text{fit parameter}} \quad \frac{\Delta k l_{ee}}{2} \right) \quad (6.42)$$

and the fit yields

$$\frac{2v_f \tau_\phi}{l_{ee}} \simeq 4.337 \quad \Rightarrow \quad v_f \tau_\phi \simeq 2.168 l_{ee}. \quad (6.43)$$

The second mapping yields a result which is significantly different than the first one, the results differ by a factor of roughly 2. Nevertheless, both mappings are of the same order, so we can accept this result.

We have plotted the  $p_i$  in fig. 6.6, solid lines are the  $p_i^{phen}$ , crosses the  $p_i^{micro}$ . The two curves fit remarkably good, the phenomenological model describes the microscopic one very good for small values of  $\Delta k l_{ee}$  as well as for large ones. Notice that we have performed only one single fit for all 4 plots. This explains the slight deviations of the two models in the asymptotic limit  $\Delta k \rightarrow \infty$ . However, there is still a region of  $\Delta k l_{ee}/2 \in [0.5, 2]$  where the microscopic model performs some oscillations which cannot be seen in the phenomenological one (a plot of this region is presented in fig. 6.7). These are nonetheless small deviations and can be safely ignored when concentrating on the essential physics.

In conclusion, we have shown that the phenomenological approach is a very good approximation of the microscopic one. In order to analyze the results it is therefore sufficient to look at  $\sigma_{WL}^{phen}$ . Moreover, we have found a connection between  $\tau_\phi$  and  $l_{ee}$

$$v_f \tau_\phi \simeq 2.168 l_{ee}, \quad v_f \tilde{\tau}_\phi \simeq 1.069 l_{ee}, \quad (6.44)$$

and since  $l_{ee} \simeq v_f^2/gT$ , we have now a connection between  $\tau_\phi$  and the tunable parameters interaction strength  $g$  (given in eq. (6.22)) and temperature  $T$ .

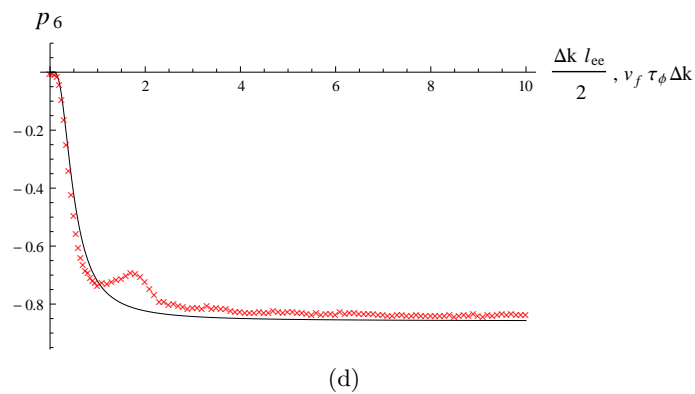
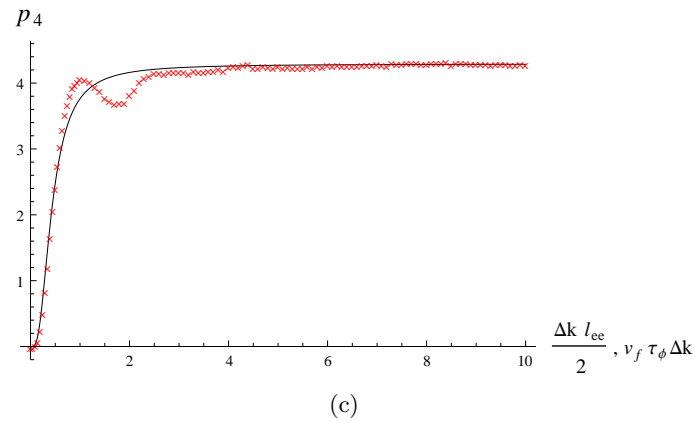
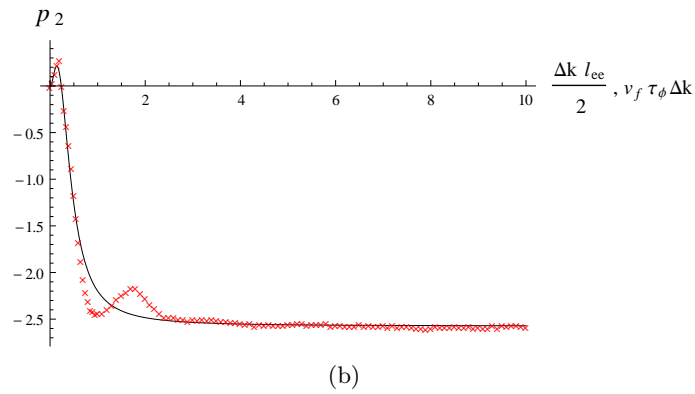
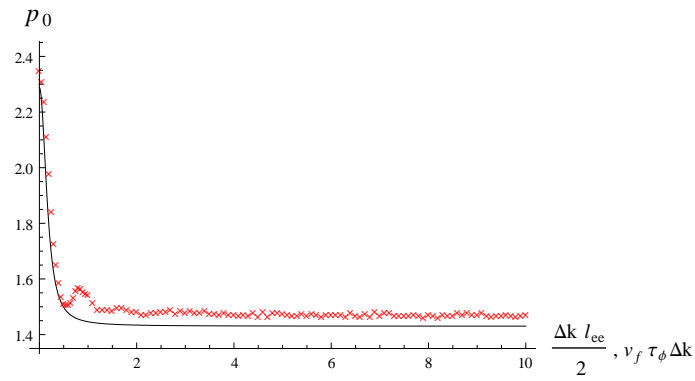


Figure 6.6.: Fitting of the analytics with the numerics for every  $p_i$ . Solid line is the analytic result from the phenomenological model, red crosses are the numerical results from the microscopic one. (a) is the plot of  $p_0$ , (b) of  $p_2$ , (c) of  $p_4$ , (d) of  $p_6$ .

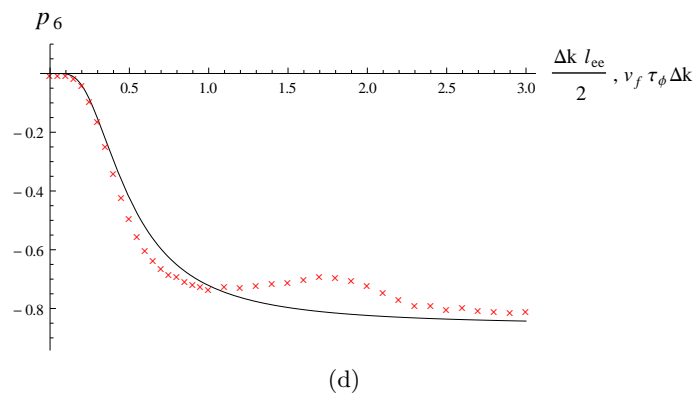
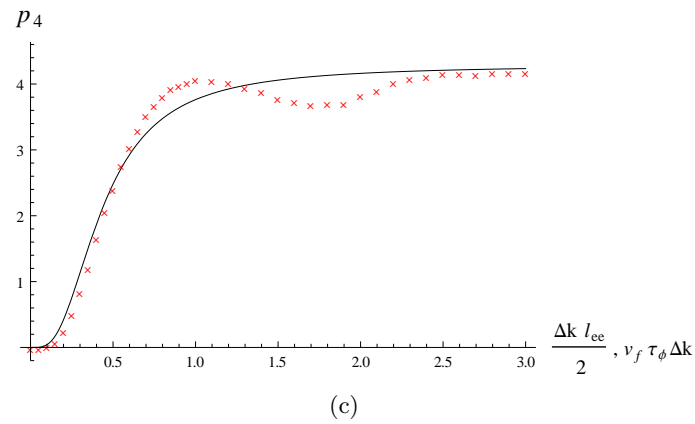
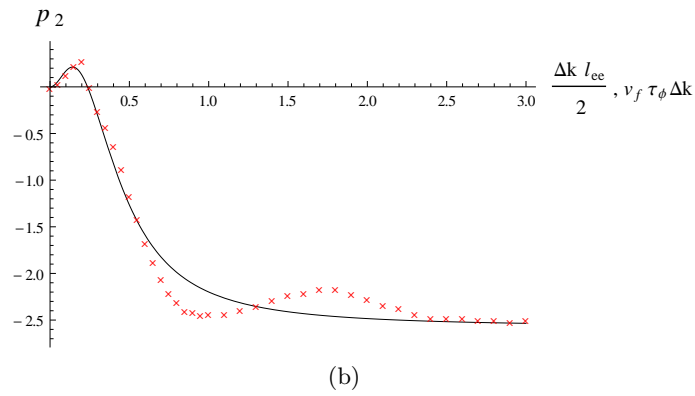
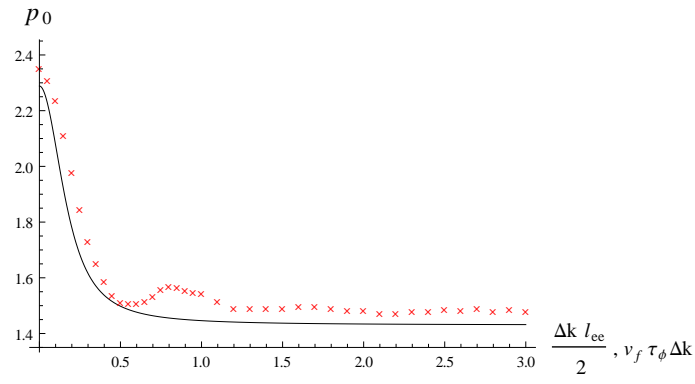


Figure 6.7.: Fitting of the analytics with the numerics for every  $p_i$ , but zoomed to see the details of the plot. The properties are the same as in fig. 6.6.



## 7. Results

In the last chapter, we have calculated the weak localization correction for the 2-chain ladder. We have seen that the phenomenological model is a good approximation of the microscopic one, so we analyze the former. The correction is given by

$$\sigma_{WL} = -\frac{1}{8}\sigma_D \left(\frac{\tau_\phi}{\tau}\right)^2 K(\tau_\phi, t_\perp, f), \quad (7.1)$$

with  $K(\tau_\phi, t_\perp, f)$  presented in eq. (6.14). The single chain has been calculated by [19], their result is

$$\sigma_{WL} = -\frac{1}{8}\sigma_D \left(\frac{\tau_\phi}{\tau}\right)^2, \quad (7.2)$$

this is just the result of our calculation for the case  $K = 1$ . Our analysis focuses on  $K(\tau_\phi, t_\perp, f)$ , because all relevant parameters are included in this function and the results can easily be compared to the single chain.

When we look at our model, we identify 2 time scales which are important:  $\tau_\phi$  and  $1/t_\perp$ . The dephasing time  $\tau_\phi$  is the time until phase coherence is destroyed by electron-electron-interaction and it determines the size of the electron loops, so it serves as a cutoff. The inverse hopping rate  $1/t_\perp = \tau_\perp$  is the average time between two interchain hopping events. In-chain hopping doesn't exhibit a hopping time because due to the linearization of the spectrum we also made the single chains continuous (see chapter 5 for details).

A closer look at  $K(\tau_\phi, t_\perp, f)$  shows that the function can be expressed in terms of two dimensionless variables:

$$\tau_\phi t_\perp, \quad \frac{v_f \pi f}{t_\perp}. \quad (7.3)$$

This shows us that the physical relevant parameters are the dephasing time  $\tau_\phi$  and the magnetic flux  $f$ . Every possible configuration of  $K$  can be achieved by varying the two relevant parameters, whereas  $t_\perp$  and  $v_f$  just define the scale.

Let us briefly recall the effects we expect from weak localization as explained in sec. 2.3. Electrons can perform loops in disordered solids, which can lead to a weak localization due

to constructive interference. The magnetic field destroys this constructive interference, the localization effect thus vanishes. We also stated that dephasing determines the size of the loops and that the effect becomes stronger in lower dimensions.

We start our analysis by looking at the limits of our  $K$ .

- **Limit of no interchain hopping**

$$K(\tau_\phi, t_\perp = 0, f) = 2 \quad (7.4)$$

This is a reasonable result because it is just the result of 2 independent chains, as compared with eq. (7.2). Note that the result is independent of magnetic flux, this is also reasonable because without interchain hopping loops cannot include an area containing magnetic field.

- **Limit of strong dephasing**

$$K(\tau_\phi = 0, t_\perp, f) = 2 \quad (7.5)$$

The limit of strong dephasing also leads to the result of two decoupled chains. As mentioned before, dephasing time, or the according dephasing length  $l_\phi = v_f \tau_\phi$ , determines the size of the electron loop. The dephasing time goes to zero in the limit of strong dephasing, in consequence we also have no dephasing length and the size of the loops becomes zero. Since we have a finite spacing between the chains, loops containing hopping cannot exist and we are therefore left with loops containing only impurities on one chain. However, this limit is obsolete since the correction vanishes completely as seen in eq. (7.1).

- **Limit of no magnetic field**

$$K(\tau_\phi, t_\perp, f = 0) = \frac{1}{4} \left[ 5 + \frac{1}{1 + (2t_\perp \tau_\phi)^2} + \frac{2}{(1 + (2t_\perp \tau_\phi)^2)^2} \right] \quad (7.6)$$

In this case we don't get the result of two independent chains in general. In the limit  $\tau_\phi \rightarrow 0$  or  $t_\perp \rightarrow 0$  we get  $K = 2$ , so we recover again the previous limits. In the case of  $\tau_\phi \rightarrow \infty$  or  $t_\perp \rightarrow \infty$  we get  $K = 5/4$ , so the correction is still stronger than in

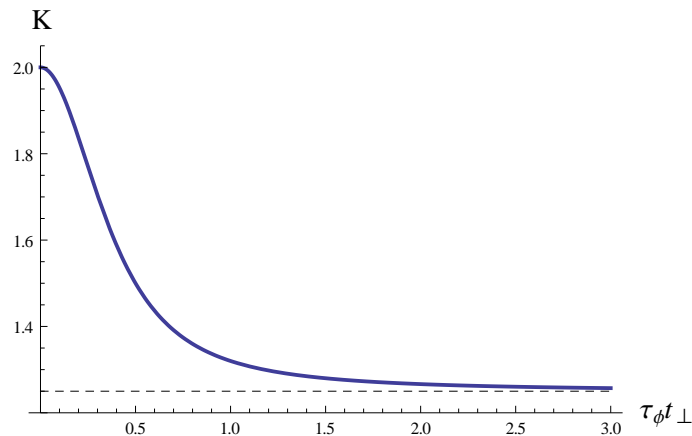


Figure 7.1.: Plot of  $K$  over  $\tau_\phi t_\perp$  in the limit of no magnetic field. Solid line is  $K$ , dashed line is at  $K = 5/4$  and denotes the asymptotic behaviour of  $K$  for large values of  $\tau_\phi t_\perp$ .

the case of a single chain. A plot of this function is given in fig. 7.1. However, the origin of the value  $K = 5/4$  is still not understood.

Note that for  $t_{\perp} \neq 0$  and  $\tau_{\phi} \neq 0$ , the correction is smaller than two. This means that the localization in the two-chain-ladder is less pronounced than in the case of two uncoupled chains. An explanation for this result can be found in dimensionality: By adding a second chain separated by a finite spacing we destroy the one-dimensionality of our system and go a little bit into two dimensions. In section 2.3 we stated that localization is stronger in lower dimensions, so our result is perfectly fine with this statement. However, one can also give a more physical interpretation: Since our model contains two bands with different Fermi points  $k_{f,\pm}$ , scattering off an impurity can lead to each of the two bands. This can lead to less coherent contributions when two ways (regular and time-reversed) occupy different bands.

We can also give an expansion of  $K(\tau_{\phi}, t_{\perp}, f)$  for small magnetic fields:

$$K(\tau_{\phi}, t_{\perp}, f) = \frac{1}{4} \left[ 5 + \frac{1}{1 + (2\tau_{\phi}t_{\perp})^2} + \frac{2}{(1 + (2\tau_{\phi}t_{\perp})^2)^2} + \left( \frac{v_f \pi f}{t_{\perp}} \right)^2 \left( -9 + \frac{192}{(4 + (2\tau_{\phi}t_{\perp})^2)^2} + \frac{32}{4 + (2\tau_{\phi}t_{\perp})^2} + \frac{4}{(1 + (2\tau_{\phi}t_{\perp})^2)^3} - \frac{5}{(1 + (2\tau_{\phi}t_{\perp})^2)^2} - \frac{10}{1 + (2\tau_{\phi}t_{\perp})^2} \right) + \mathcal{O} \left[ \frac{v_f \pi f}{t_{\perp}} \right]^4 \right] \quad (7.7)$$

- **Limit of a strong magnetic field**

$$K(\tau_{\phi}, t_{\perp}, f \rightarrow \infty) = 2 \quad (7.8)$$

In the limit of a strong magnetic field we find again the limit of two uncoupled chains. This totally contradicts our expectation because due to our knowledge (see section 2.3), magnetic field should suppress localization and the correction should therefore become smaller. In our case, however, magnetic field makes the correction even stronger, it forces electrons to localize.

According to this result, the magnetic field seems to split the chains again into two uncoupled ones. Having said this, the first idea is to look at the hopping itself. When adding a magnetic field, the interchain hopping parameter becomes renormalized by means of the Peierls substitution

$$t_{\perp} \rightarrow t_{\perp} \exp[\mp i 2\pi f x]. \quad (7.9)$$

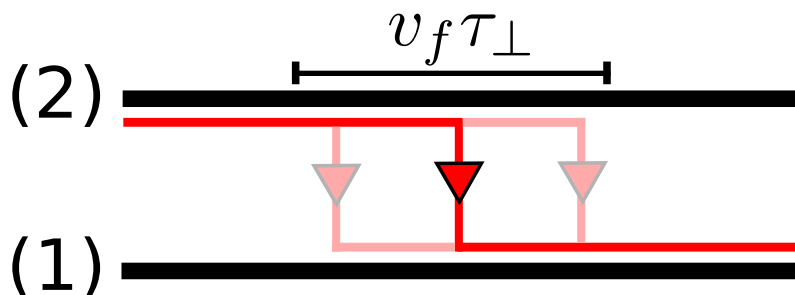


Figure 7.2.: Hopping in the continuous ladder. Interchain hopping can take place on a scale of  $l_{\perp} = v_f \tau_{\perp}$ .

This substitution has been done in detail in section 5.2. Since we have linearized our model, we have made the two chains continuous. We thus do not know exactly where the interchain hopping occurs, we just know it occurs on a scale of  $l_{\perp} = v_f \tau_{\perp}$ . In this spirit, we have to average over all possible hopping events on a length scale of  $l_{\perp}$ , as shown in fig. 7.2. This leads to a renormalized hopping parameter

$$\tilde{t}_{\perp} = \int \frac{dx}{l_{\perp}} t_{\perp} e^{i2\pi f x} P\left(\frac{x}{l_{\perp}}\right), \quad (7.10)$$

with a probability distribution  $P(x)$ . The renormalized hopping parameter is depending on the magnetic field  $\tilde{t}_{\perp} = \tilde{t}_{\perp}(f l_{\perp})$  and becomes smaller with increasing magnetic field. This effect can also be interpreted as destructive interference between different hopping events.

However, the decoupling of the 2 chains can already be seen in the derivation of the ladder model in sec. 5.2. The inter-chain propagator reads

$$G_{\perp} = \frac{1}{2} \sqrt{1 - \alpha^2} (G_{+} - G_{-}), \quad \alpha = \frac{v_f \pi f}{\sqrt{(v_f \pi f)^2 + t_{\perp}^2}}. \quad (7.11)$$

In the limit of  $f \rightarrow \infty$ ,  $\alpha \rightarrow 1$  and consequently  $G_{\perp} \rightarrow 0$ .

It is still worth mentioning that the limit of infinite magnetic field has to be taken with care. In this limit it is not guaranteed that one can linearize the spectrum, therefore the whole calculation cannot be trusted anymore. However, this limit still yields a lot of useful information about our model.

The expansion of  $K(\tau_{\phi}, t_{\perp}, f)$  for large magnetic field reads

$$K(\tau_{\phi}, t_{\perp}, f) = 2 - 3 \frac{1}{\left(\frac{v_f \pi f}{t_{\perp}}\right)^2} + \frac{1}{\left(\frac{v_f \pi f}{t_{\perp}}\right)^4} \left(\frac{9}{2} + \frac{1}{(\tau_{\phi} t_{\perp})^2}\right) + \mathcal{O}\left[\frac{1}{\left(\frac{v_f \pi f}{t_{\perp}}\right)^6}\right]. \quad (7.12)$$

It is noteworthy that the first appearance of  $\tau_{\phi}$  is in the 4th order of this expansion. The 2nd order expansion is just given by a number, the behaviour of  $K$  for large magnetic fields thus depends very weakly on  $\tau_{\phi}$ .

In order to get a more quantitative analysis of the conductivity correction one can introduce a new dimensionless conductivity correction

$$\delta\sigma(\tau_{\phi}, t_{\perp}, f) = \frac{\sigma_{WL}(\tau_{\phi}, t_{\perp}, f) - \sigma_{WL}(\tau_{\phi}, t_{\perp}, 0)}{\sigma_{WL}(\tau_{\phi}, t_{\perp}, 0)} \quad (7.13)$$

where  $\sigma_{WL}$  is given by eq. (6.13).  $\delta\sigma$  has been plotted for multiple values of  $\tau_{\phi} t_{\perp}$  in fig. 7.3. The different scales on the  $\delta\sigma$ -axis are due to the different values of  $\sigma_{WL}(\tau_{\phi}, t_{\perp}, 0)$  depending on  $\tau_{\phi}$ .

As stated above, all plots approach an asymptotic limit in the case of  $f \rightarrow \infty$ . From the plots in fig. 7.3 we can see that this asymptotic limit is reached faster for higher values of  $\tau_{\phi} t_{\perp}$ . However, in the cases of high  $\tau_{\phi} t_{\perp}$ , a minimum appears for small magnetic field. It is apparent that the strength of this minimum grows with  $\tau_{\phi} t_{\perp}$ , but it seems that it becomes saturated at  $\tau_{\phi} t_{\perp} \simeq 1.5$ .

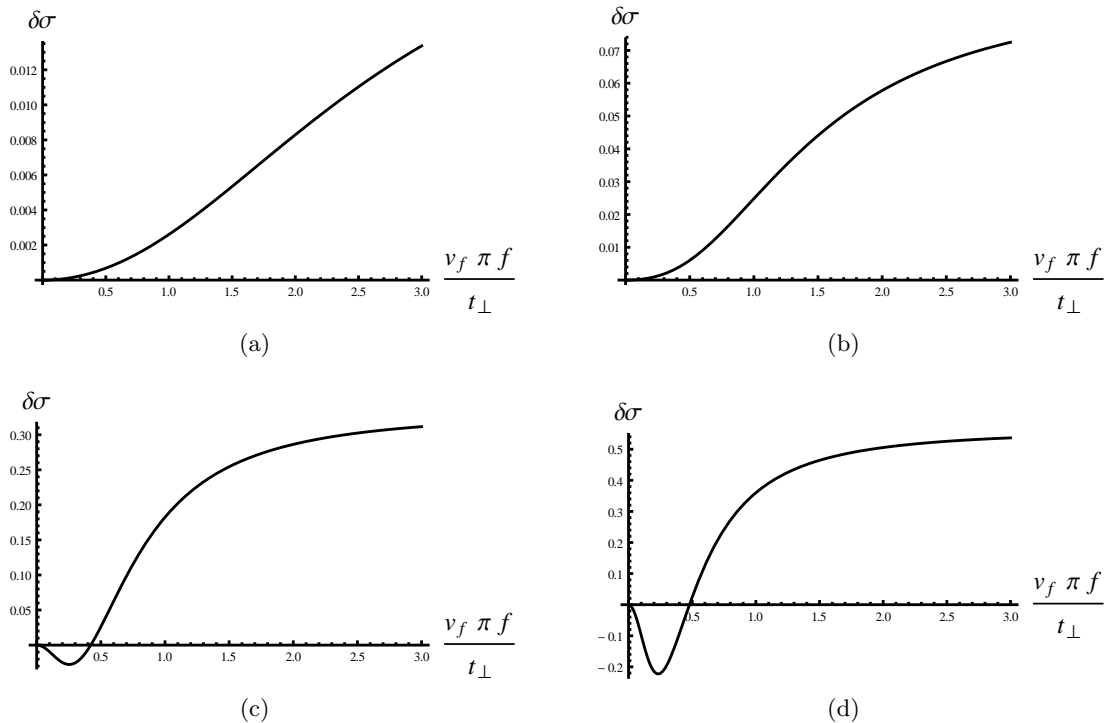


Figure 7.3.: Plots of  $\delta\sigma$  over the generalized magnetic field  $\frac{v_f \pi f}{t_\perp}$  for various values of  $\tau_\phi t_\perp$ .  
 (a)  $\tau_\phi t_\perp = 0.1$ ; (b)  $\tau_\phi t_\perp = 0.2$ ; (c)  $\tau_\phi t_\perp = 0.5$ ; (d)  $\tau_\phi t_\perp = 1.5$ .

This minimum reflects the fact that we obtain a magnetoresistance which we expected by weak localization. It seems that for large enough dephasing times the electron can perform a loop and therefore leads to the regular weak localization correction. However, this only holds for small magnetic fields, large magnetic fields still lead to the splitting of the 2 chains and suppress the regular weak localization correction.

The development of the minimum can be seen in the expansion of  $K$  for small  $f$ , eq. (7.7). The lowest order expansion consists of different competing terms, which determine the overall sign. A sign change of the 2nd order expansion denotes the appearance of a minimum, the sign change appears at

$$\tau_\phi t_\perp \simeq 0.266. \quad (7.14)$$

In the limit of weak dephasing  $\tau_\phi \rightarrow \infty$  we find that the minimum is at

$$\left. \frac{v\pi f}{t_\perp} \right|_{min} = \frac{1}{\sqrt{2}} \quad (7.15)$$

with the value

$$\delta\sigma \Big|_{min} = -\frac{13}{45} \quad \text{or} \quad K \Big|_{min} = \frac{8}{9}. \quad (7.16)$$

The limit of  $\tau_\phi \rightarrow \infty$  has to be taken with care, since the whole calculation has been performed under the assumption  $\tau_\phi \ll \tau$ . Nonetheless, the numerical data shows that these limits are reached quite fast, so taking the limit  $\tau_\phi \rightarrow \infty$  is valid in this case.

However, the regular weak localization correction can only be observed for small magnetic fields. Large magnetic field leads still to a decoupling of the two chains and therefore *enhances* the localization.

## 8. Conclusion

The main goal of this thesis was to calculate the weak localization correction to the conductivity of a spinless disordered 2-chain ladder.

In chapter 5 we have introduced the cornerstone of this thesis, the model of a 2-chain ladder. In absence of a magnetic field the bandstructure consists of two cosine bands, split by a factor of  $\Delta\epsilon = 2t_\perp$ . The bandstructure has been linearized, we assumed that both linear bands have the same Fermi velocity  $v_f$ . Adding a magnetic field results in two effects: The momentum difference between the two bands,  $\Delta k$ , becomes renormalized, furthermore one has to include a coherence factor  $\alpha$  in the Greens function.

The actual calculation of the weak localization correction has been performed in chapter 6. We have calculated the correction in a phenomenological model, which has been validated afterwards by a microscopic one. Furthermore, we have found a mapping of the phenomenological dephasing time  $\tau_\phi$  on the microscopic electron-electron scattering length  $l_{ee} \simeq v_f^2/gT$  of the form  $v_f\tau_\phi \sim l_{ee}$ . This mapping provides a connection between the phenomenological model and system-inherent quantities like the interaction strength  $g$  and the temperature  $T$ .

Chapter 7 is devoted to the examination and discussion of the results obtained in chapter 6. The weak localization correction to the 2-chain ladder is given by

$$\sigma_{WL} = -\frac{1}{8}\sigma_D \left(\frac{\tau_\phi}{\tau}\right)^2 K(\tau_\phi, t_\perp, f), \quad (8.1)$$

where the function  $K(\tau_\phi, t_\perp, f)$  is given in eq. (6.14). The analysis of the correction focuses on  $K(\tau_\phi, t_\perp, f)$ , since all relevant parameters are included in this function. In the limit of no interchain hopping, the result of two uncoupled chains has been recovered, in agreement with [19]. In the absence of a magnetic field, the weak localization correction of the 2-chain ladder is smaller than for the case of two uncoupled chains.

A surprising result is yielded in the case of strong magnetic fields. Magnetic field apparently suppresses interchain hopping and leads to decoupling of the two chains. Consequently, the weak localization correction becomes stronger with increasing magnetic field. The suppression of interchain hopping can be explained in terms of destructive interference of different hopping paths. Another interesting effect can be seen at large dephasing times  $\tau_\phi \gtrsim t_\perp^{-1}$  (but still in the limit  $\tau_\phi \ll \tau$ ). In this regime one can observe a competition between the regular weak localization correction (seen at small magnetic fields  $f \lesssim \pi t_\perp/2v_f$ ) and the decoupling of the chains (large magnetic fields).

After finishing the thesis there are still some unresolved questions. The most fundamental one addresses to the mechanism which decouples the chains in the magnetic field. Although an explanation has been given, it is still crucial to put the given statements on solid ground. Furthermore, the limit of strong interchain hopping in the absence of magnetic field leads to a result which is not fully understood.

Future work based on this thesis can be addressed to the analysis of carbon nanotubes, for example. Single wall carbon nanotubes can be mapped onto the 2-chain ladder [24]. This mapping does not hold completely in the presence of the magnetic field, in this case the geometric structure of the nanotube has to be considered. Nevertheless, the calculation of the weak localization correction of carbon nanotubes should be quite similar to the one of the 2-chain ladder. In fact, a regular weak localization correction has been measured in single wall carbon nanotubes [26]. This measurement is in contrast to the results of this thesis, which makes the analysis of carbon nanotubes even more interesting. However, further work must be done to make any reasonable comment on this.

The low-temperature limit of 2-chain ladders also promises exciting physics. The case of up to two impurities has already been investigated [10] and shows interesting results, consequently one is interested in the case of many impurities. More interesting effects are expected by the competition between strong localization and backscattering off disorder, which leads to a formation of a gap.

# Deutsche Zusammenfassung

## Motivation

Eindimensionale Systeme ziehen schon lange das Interesse der Physiker auf sich. Luttinger und Tomonaga waren die Ersten, die in den 50er Jahren versuchten eindimensionale Systeme theoretisch zu behandeln, indem sie eine neues Modell namens Luttinger Flüssigkeit vorschlugen [25, 35]. Ihre Arbeit hat gezeigt, dass sich eindimensionale Systeme deutlich anders verhalten als Höherdimensionale. Diese Ergebnisse haben ein verstärktes Interesse der theoretischen Physik an 1D Systemen hervorgerufen.

Es hat Jahrzehnte gedauert, bis erste experimentelle Realisierungen eindimensionaler Systeme verfügbar waren, aber mittlerweile gibt es zahlreiche Beispiele. Die Bekanntesten sind Kohlenstoff-Nanoröhrchen [7], halbleitende und metallische Nanodrähte [5, 23, 33] und die Randzustände des Quanten-Hall-Effekts [21]. Kohlenstoff-Nanoröhrchen haben hierbei die größte Aufmerksamkeit erhalten, wobei Experimente das typische Verhalten einer Luttinger Flüssigkeit gezeigt haben.

Ein sehr interessantes Feld der Festkörperphysik ist das der ungeordneten Systeme. Anderson hat 1958 gezeigt, dass Unordnung zur Lokalisierung von Elektronen führen kann [3], aber es hat mehr als 20 Jahre gedauert um die Theorie der Lokalisierung zu entwickeln [1]. Diese zeigt, dass die Stärke der Lokalisierung stark von der Dimensionalität des Systems abhängt und der Effekt in einer Dimension besonders stark ausgeprägt ist.

Obwohl die reinen, wechselwirkenden 1D-Systeme (Luttinger Flüssigkeiten) und die ungeordneten, nicht-wechselwirkenden 1D-Systeme (die zu Lokalisierung führen) sehr gut verstanden sind, ist immer noch wenig bekannt über die Natur ungeordneter, wechselwirkender 1D-Systeme (ungeordnete Luttinger Flüssigkeit). Systeme mit einer einzigen Störstelle wurden extensiv untersucht [20], viel problematischer ist jedoch der Fall vieler Störstellen. Die ersten Versuche, ungeordnete Luttinger Flüssigkeiten zu behandeln wurden von Apel und Rice [4] und von Giamarchi und Schulz [17] vorangetrieben, mittlerweile gibt es jedoch große Fortschritte auf diesem Gebiet [6, 19].

Ein interessanter Effekt, der durch Unordnung hervorgerufen wird, ist schwache Lokalisierung. Schwache Lokalisierung ist ein quantenmechanisches Interferenzphänomen zwischen verschiedenen Pfaden, die eine geschlossene Schleife bilden, und führt zu Quantenlokalisierung und zu einer Verringerung der Leitfähigkeit. Die Stärke der Lokalisierung wird bestimmt durch die Stärke der Kohärenz, diese wiederum kann z.B. durch inelastische Streuung zerstört werden. Diesen Effekt nennt man Dephasierung und er führt eine neue Größe, die Dephasierungszeit  $\tau_\phi$ , ein. Diese Dephasierungszeit hängt von externen Größen wie der Wechselwirkungsstärke und der Temperatur ab, aber die parametrische Form dieses Zusammenhangs wird von der Dimensionalität des Systems bestimmt. Darüber hinaus hängt die Stärke der Lokalisierung von äußeren Magnetfeldern ab. Ein angelegtes Magnetfeld zerstört den Interferenzeffekt und führt zu einer Schwächung des Lokalisierungseffekts.

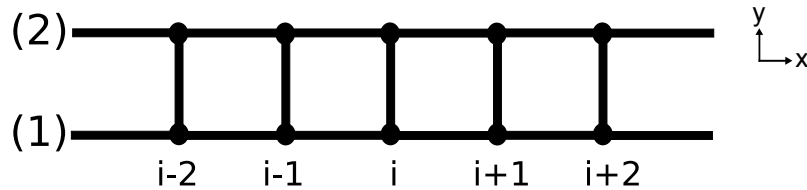
Das Ziel dieser Diplomarbeit ist es, die Korrektur der schwachen Lokalisierung zur Leitfähigkeit einer spinlosen, ungeordneten Leiter zu berechnen. Wir beschränken uns hierzu

auf den Grenzfall der starken Dephasierung,  $\tau_\phi \ll \tau$ , dieser Fall kann durch eine genügend schwache Unordnung oder eine ausreichend hohe Temperatur gewährleistet werden. Die Leitfähigkeitskorrektur ist aus mehreren Gründen interessant: Zum einen wurde die Korrektur der schwachen Lokalisierung für einzelne 1D-Drähte schon berechnet [19, 37] und es ist der sinnvollste Schritt, das System auf eine Leiter auszudehnen. Desweiteren ist die Leiter eines der einfachsten eindimensionalen Systeme, in denen schwache Lokalisierung zu Magnetowiderstand führen kann. Dies ist nicht möglich in spinlosen 1D-Drähten, da das Magnetfeld in diesen Systemen immer weggeegicht werden kann. 1D-Drähte mit Spin können jedoch Magnetowiderstand aufweisen, der zugrunde liegende Mechanismus ist hier der Zeeman-Effekt [36, 38].

Ferner können Kohlenstoff-Nanoröhrchen auf die Leiter abgebildet werden [24]. Experimente haben gezeigt, dass Kohlenstoff-Nanoröhrchen Magnetowiderstand aufzeigen, dessen Ursprung der schwachen Lokalisierung zugeschrieben wird [26]. Die Abbildung auf die Leiter ist jedoch im Magnetfeld nicht mehr so ohne weiteres möglich, in diesem Fall muss die geometrische Struktur der Nanoröhrchen berücksichtigt werden. Nichtsdestotrotz liefert diese Diplomarbeit die Grundlagen, um die Leitfähigkeitskorrektur der schwachen Lokalisierung in Kohlenstoff-Nanoröhrchen zu berechnen.

## Modell

In dieser Diplomarbeit untersuchen wir die folgende Leiterstruktur:



In dieser Abbildung stehen Punkte für Gitterpositionen und die Linien zeigen die möglichen Hüpfrihtungen an. Die Dispersionsrelation der Leiter ist gegeben durch zwei Cosinusförmige Bänder  $+/-$  mit einem konstanten Abstand  $\Delta\epsilon = 2t_\perp$ . Da wir nur an Anregungen in der Nähe der Fermikante interessiert sind, linearisieren wir die beiden Dispersionsrelationen unter der Annahme, dass beide Bänder die gleiche Fermigeschwindigkeit  $v_f$  besitzen. Unter dieser Annahme sind die beiden linearisierten Bänder allein durch die beiden Fermi-Impulse  $k_{f,\pm}$  charakterisiert.

Ein angelegtes äußeres Magnetfeld führt zu einer Renormierung dieser Fermi-Impulse, bzw. der Differenz der beiden Impulse  $\Delta k = k_{f,+} - k_{f,-}$ . Das Magnetfeld erhöht diese Differenz und schiebt somit die beiden Bänder auseinander. Darüber hinaus führt es zu sogenannten Kohärenz-Faktoren  $\alpha$  in den Greens-Funktionen. Die genaue Form dieser Faktoren kann Gl. (5.23) entnommen werden.

## Berechnung der Leitfähigkeitskorrektur

Die Leitfähigkeitskorrektur wird in dieser Diplomarbeit auf zweierlei Art berechnet. Zunächst wird die Wechselwirkung auf eine approximative Art berücksichtigt, indem eine phänomenologische Dephasierungszeit  $\tau_\phi$  eingeführt wird. Dieser Ansatz hat den Vorteil einer einfachen Rechnung und führt schließlich zu einem analytischen Ergebnis. Der zweite Ansatz benutzt die Technik der funktionalen Bosonisierung, um die Wechselwirkung auf

einem mikroskopischen Niveau zu behandeln. Diese Methode ist mathematisch weitaus schwieriger als die Phänomenologische und liefert als Ergebnis ein schwieriges Integral, das numerisch ausgewertet werden muss.

Ein Vergleich der beiden Methoden zeigt, dass das phänomenologische Modell das Mikroskopische sehr gut beschreibt. Darüber hinaus finden wir eine Verknüpfung der phänomenologischen Dephasierungszeit mit der Elektron-Elektron-Streulänge  $l_{ee}$  der Form  $v_f \tau_\phi \sim l_{ee}$ . Die Elektron-Elektron-Streulänge ist dabei mit der Wechselwirkungsstärke  $g$  und der Temperatur  $T$  über die Beziehung  $l_{ee} \simeq v_f^2/gT$  verknüpft. Dies gibt uns die Möglichkeit, die Dephasierungszeit durch äußere Bedingungen zu steuern.

## Diskussion der Leitfähigkeitskorrektur

Im Grenzfall starker Dephasierung  $\tau_\phi \ll \tau$  erhält man für die Leitfähigkeitskorrektur

$$\sigma_{WL} = -\frac{1}{8}\sigma_D \left(\frac{\tau_\phi}{\tau}\right)^2 K(\tau_\phi, t_\perp, f),$$

wobei  $\sigma_D$  die Drude-Leitfähigkeit ist und  $K(\tau_\phi, t_\perp, f)$  durch Gl. (6.14) gegeben ist. Die Analyse dieses Ergebnisses konzentriert sich größtenteils auf die Funktion  $K(\tau_\phi, t_\perp, f)$ , da sie alle wichtigen physikalischen Variablen enthält. Wenn das Hüpfen zwischen den beiden 1D-Drähten der Leiter verboten wird, also  $t_\perp \rightarrow 0$ , erhält man in Übereinstimmung mit [19] den Fall zweier unabhängiger 1D-Drähte. Ohne Magnetfeld ist die Leitfähigkeitskorrektur der Leiter kleiner als die der zwei unabhängigen Drähte.

Im Falle starker Magnetfelder erhält man wieder den Fall der beiden ungekoppelten Drähte, das Magnetfeld verstärkt also die Lokalisierung. Dies ist ein überraschendes Resultat, normalerweise führt das Magnetfeld zu einer Abschwächung der Lokalisierung. Anscheinend interferieren verschiedene Hüpfprozesse destruktiv im Falle eines starken Magnetfelds, was zu einer effektiven Entkopplung der beiden Drähte führt. Für genügend große Dephasierungszeiten  $\tau_\phi \gtrsim t_\perp^{-1}$  (wobei immer noch  $\tau_\phi \ll \tau$  gelten muss) kann die erwartete Korrektur der schwachen Lokalisierung beobachtet werden, jedoch nur im Falle ausreichend kleiner Magnetfelder  $f \lesssim \pi t_\perp/2v_f$ . Starke Magnetfelder führen wieder zu einer Entkopplung der beiden Drähte, was dazu führt dass man einen Wettstreit zweier konkurrierender Effekte beobachten kann.

Während der Diplomarbeit konnten nicht alle Fragen geklärt werden. Vor allem der Mechanismus, der zur Entkopplung der beiden Drähte im starken Magnetfeld führt muss stärker untersucht werden. Wir haben zwar eine qualitative Erklärung gegeben, diese muss jedoch noch durch eine ausführliche Rechnung bestätigt werden.

## Ausblick

Die Untersuchung von Kohlenstoff-Nanoröhrchen ist eine naheliegende Fortsetzung dieser Diplomarbeit, da diese auf die Leiter abgebildet werden können [24]. Experimente haben gezeigt, dass Kohlenstoff-Nanoröhrchen einen Magnetowiderstand aufweisen, der der (regulären) schwachen Lokalisierung zugeschrieben wird [26]. Diese Experimente zeigen nicht die Verstärkung der Lokalisierung, wie sie in dieser Diplomarbeit vorhergesagt wurde. Jedoch muss auch erwähnt werden, dass sich Nanoröhrchen im Magnetfeld anders verhalten als Leiterstrukturen. Ohne eine ausführliche Untersuchung kann über das Verhalten von Nanoröhrchen keine Aussage getroffen werden.

Spannende Physik wird auch bei sehr niedrigen Temperaturen in Leitermodellen erwartet. Erste Arbeiten über das Verhalten einzelner Störstellen zeigen ein interessantes Verhalten [10], folglich ist man am Verhalten der ungeordneten Leiter interessiert. Ferner erwartet man interessante Effekte beim Wettbewerb zwischen starker Lokalisierung und der Rückstreuung an Störstellen, was zur Bildung einer Bandlücke führt.

# Bibliography

- [1] E. Abrahams, P. W. Anderson, D. C. Licciardello, and T. V. Ramakrishnan. Scaling theory of localization: Absence of quantum diffusion in two dimensions. *Phys. Rev. Lett.*, 42:673–676, Mar 1979.
- [2] A. Altland and B. Simons. *Condensed matter field theory*. Cambridge University Press, 2006.
- [3] P. W. Anderson. Absence of diffusion in certain random lattices. *Phys. Rev.*, 109:1492–1505, Mar 1958.
- [4] W. Apel and T. M. Rice. Combined effect of disorder and interaction on the conductance of a one-dimensional fermion system. *Phys. Rev. B*, 26:7063–7065, Dec 1982.
- [5] O. M. Auslaender, A. Yacoby, R. de Picciotto, K. W. Baldwin, L. N. Pfeiffer, and K. W. West. Experimental evidence for resonant tunneling in a luttinger liquid. *Phys. Rev. Lett.*, 84:1764–1767, Feb 2000.
- [6] D.M. Basko, I.L. Aleiner, and B.L. Altshuler. Metal–insulator transition in a weakly interacting many-electron system with localized single-particle states. *Annals of Physics*, 321(5):1126 – 1205, 2006.
- [7] Marc Bockrath, David H. Cobden, Jia Lu, Andrew G. Rinzler, Richard E. Smalley, Leon Balents, and Paul L. McEuen. Luttinger-liquid behaviour in carbon nanotubes. *Nature*, 397(6720):598–601, Feb 1999.
- [8] H. Bruus and K. Flensberg. *Many-body quantum theory in condensed matter physics: an introduction*. Oxford graduate texts in mathematics. Oxford University Press, 2004.
- [9] Sam T. Carr, Boris N. Narozhny, and Alexander A. Nersesyan. Spinless fermionic ladders in a magnetic field: Phase diagram. *Phys. Rev. B*, 73(19):195114, May 2006.
- [10] Sam T. Carr, Boris N. Narozhny, and Alexander A. Nersesyan. Effect of a local perturbation in a fermionic ladder. *Phys. Rev. Lett.*, 106:126805, Mar 2011.
- [11] Piers Coleman. *Introduction to Many Body Physics*. 2011.
- [12] V. V. Deshpande, M. Bockrath, L. I. Glazman, and A Yacoby. Electron liquids and solids in one dimension. *Nature*, 464:209, March 2010.
- [13] I.E. Dzyaloshinskii and A.I. Larkin. Correlation functions for a one-dimensional fermi system with long-range interaction (tomonaga model). 38(1), 1974.
- [14] A. Enayati-Rad, A. Narduzzo, F. Rullier-Albenque, S. Horii, and N. E. Hussey. Irradiation-induced confinement in a quasi-one-dimensional metal. *Phys. Rev. Lett.*, 99:136402, Sep 2007.
- [15] H C Fogedby. Correlation functions for the tomonaga model. *Journal of Physics C: Solid State Physics*, 9(20):3757, 1976.

- [16] T. Giamarchi. *Quantum physics in one dimension*. International series of monographs on physics. Clarendon, 2004.
- [17] T. Giamarchi and H. J. Schulz. Anderson localization and interactions in one-dimensional metals. *Phys. Rev. B*, 37:325–340, Jan 1988.
- [18] A.O. Gogolin, A.A. Nersesyan, and A.M. Tsvelik. *Bosonization and strongly correlated systems*. Cambridge University Press, 2004.
- [19] I. V. Gornyi, A. D. Mirlin, and D. G. Polyakov. Electron transport in a disordered luttinger liquid. *Phys. Rev. B*, 75(8):085421, Feb 2007.
- [20] C. L. Kane and Matthew P. A. Fisher. Transport in a one-channel luttinger liquid. *Phys. Rev. Lett.*, 68:1220–1223, Feb 1992.
- [21] W. Kang, H. L. Stormer, L. N. Pfeiffer, K. W. Baldwin, and K. W. West. Tunnelling between the edges of two lateral quantum hall systems. *Nature*, 403(6765):59–61, Jan 2000.
- [22] D K K Lee and Y Chen. Functional bosonisation of the tomonaga-luttinger model. *Journal of Physics A: Mathematical and General*, 21(22):4155, 1988.
- [23] E. Levy, A. Tsukernik, M. Karpovski, A. Palevski, B. Dwir, E. Pelucchi, A. Rudra, E. Kapon, and Y. Oreg. Luttinger-liquid behavior in weakly disordered quantum wires. *Phys. Rev. Lett.*, 97:196802, Nov 2006.
- [24] Hsiu-Hau Lin. Correlation effects of single-wall carbon nanotubes in weak coupling. *Phys. Rev. B*, 58:4963–4971, Aug 1998.
- [25] J. M. Luttinger. An exactly soluble model of a many?fermion system. 4(9):1154–1162, 1963.
- [26] H. T. Man and A. F. Morpurgo. Sample-specific and ensemble-averaged magnetoconductance of individual single-wall carbon nanotubes. *Phys. Rev. Lett.*, 95:026801, Jul 2005.
- [27] Daniel C. Mattis and Elliott H. Lieb. Exact solution of a many?fermion system and its associated boson field. 6(2):304–312, 1965.
- [28] N.F. Mott and W.D. Twose. The theory of impurity conduction. *Advances in Physics*, 10(38):107–163, 1961.
- [29] A Narduzzo, A Enayati-Rad, P J Heard, S L Kearns, S Horii, F F Balakirev, and N E Hussey. Fragile three-dimensionality in the quasi-one-dimensional cuprate prba 2 cu 4 o 8. *New Journal of Physics*, 8(9):172, 2006.
- [30] E. Orignac and T. Giamarchi. Effects of weak disorder on two coupled hubbard chains. *Phys. Rev. B*, 53:R10453–R10456, Apr 1996.
- [31] R. Peierls. Zur theorie des diamagnetismus von leitungselektronen. *Zeitschrift für Physik A Hadrons and Nuclei*, 80:763–791, 1933. 10.1007/BF01342591.
- [32] H. Schulz. Fermi liquids and non-fermi liquids. *eprint arXiv:cond-mat/9503150*, March 1995.
- [33] E. Slot, M. A. Holst, H. S. J. van der Zant, and S. V. Zaitsev-Zotov. One-dimensional conduction in charge-density-wave nanowires. *Phys. Rev. Lett.*, 93:176602, Oct 2004.
- [34] R. L. Stratonovich. On a method of calculating quantum distribution functions. *Soviet Physics Doklady*, 2:416–+, July 1957.

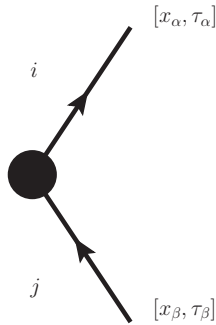
- 
- [35] S. Tomonaga. Remarks on bloch's method of sound waves applied to many-fermion problems. *Progress of Theoretical Physics*, 5(4):544–569, 1950.
- [36] A. G. Yashenkin, I. V. Gornyi, A. D. Mirlin, and D. G. Polyakov. to be published.
- [37] A. G. Yashenkin, I. V. Gornyi, A. D. Mirlin, and D. G. Polyakov. Quantum interference and spin-charge separation in a disordered luttinger liquid. *Phys. Rev. B*, 78(20):205407, Nov 2008.
- [38] Dongxiao Yue, L. I. Glazman, and K. A. Matveev. Conduction of a weakly interacting one-dimensional electron gas through a single barrier. *Phys. Rev. B*, 49:1966–1975, Jan 1994.
- [39] I. Yurkevich. Bosonisation as the hubbard-stratonovich transformation. *ArXiv Condensed Matter e-prints*, December 2001.



# Appendix

## A. Calculation of the $\mathcal{W}$ -functions

In this Appendix we calculate the  $\mathcal{W}$ -functions used in section 6.2. Note that in section 6.2 we start in the chain basis, whereas the calculation here is done in the band basis. The  $\mathcal{W}$ -functions are obtained by evaluating the diagram



Since this is the initial vertex, all Greens functions are right-movers,  $i$  and  $j$  indicate the bands. We calculate this diagram for arbitrary bands, because every combination of bands appears in the complete calculation of the Cooperon. With the definition of the Greens function

$$g_p^{R/L}(x, \tau) = \mp \frac{iT}{2v_f} \sinh^{-1} \left[ \pi T \left( \frac{x}{v_f} \pm i\tau \right) \right] \exp [\pm i k_{f,p} x], \quad (\text{A.1})$$

the diagram is given by

$$\begin{aligned} \text{Diagram} &= \int dx_i d\tau_i e^{-i\Omega\tau_i} e^{-\Gamma[|x_\alpha - x_i| + |x_\beta - x_i|]} g_i^R(x_\alpha - x_i, \tau_\alpha - \tau_i) g_j^R(x_i - x_\beta, \tau_i - \tau_\beta) \\ &= g_0^R(x_\alpha - x_\beta, \tau_\alpha - \tau_\beta) \mathcal{W}_{i,j}^{in,R}(x_\alpha, \tau_\alpha; x_\beta, \tau_\beta), \end{aligned} \quad (\text{A.2})$$

where we included a long-distance cutoff  $\Gamma = l^{-1}$ . Note that the second line forecloses a result obtained later, but it is showed here for the sake of clarity. We start with the integration over time and use the residue theorem and the Lemma of Jordan. These theorems will not be explained here, they can be looked up in lots of mathematical books.

To use the residue theorem we have to find the poles of the integrand.  $\sinh^{-1}(az)$  has poles on the imaginary axis at  $z = i\pi n/a$  with strength  $a^{-1}(-1)^n$ . In general there is

an infinite number of poles ( $n = 0, \pm 1, \pm 2, \dots$ ), but we restrict ourselves to the pole with  $n = 0$  because this pole has the biggest residue.

The Lemma of Jordan allows us to close the contour of the integral along the real axis in complex infinity, but only as long as the integrand tends fast enough to zero. The important part of the integral which needs to fulfill this condition is the  $\exp[-i\Omega\tau_i]$ -part. One can easily check that for  $\Omega > 0$  the integrand tends to zero at negative complex infinity, so the contour has to be closed in the lower half plane. Similarly, for  $\Omega < 0$  the contour has to be closed in the upper half plane.

The poles of the Greens functions can be found at

$$\tau_{i,1} = \tau_\alpha - i \frac{x_\alpha - x_i}{v_f}, \quad (\text{A.3a})$$

$$\tau_{i,2} = \tau_\beta - i \frac{x_\beta - x_i}{v_f}. \quad (\text{A.3b})$$

Note that one has to check carefully on which half plane the poles are, because the sign of  $\Omega$  tells us where to close the contour. Evaluating the integral A.2 yields

$$\begin{aligned} g_0^R(x_\alpha - x_\beta, \tau_\alpha - \tau_\beta) \mathcal{W}_{i,j}^{in,R} &= \\ &= (-1) 2\pi i \frac{-iT}{2v_f} \frac{1}{i\pi T} \int dx_i e^{-\Gamma[|x_\alpha - x_i| + |x_\beta - x_i|]} e^{ik_{f,i}(x_\alpha - x_i)} e^{ik_{f,j}(x_i - x_\beta)} \\ &\quad \left\{ -\Theta(\Omega) \left[ \Theta(x_\alpha - x_i) e^{-i\Omega\tau_\alpha - \Omega(x_\alpha - x_i)/v} \frac{-iT}{2v_f} f(\alpha - \beta) \right. \right. \\ &\quad \quad \left. \Theta(x_\beta - x_i) e^{-i\Omega\tau_\beta - \Omega(x_\beta - x_i)/v} \frac{-iT}{2v_f} f(\beta - \alpha) \right] \\ &\quad + \Theta(-\Omega) \left[ \Theta(x_i - x_\alpha) e^{-i\Omega\tau_\alpha - \Omega(x_\alpha - x_i)/v} \frac{-iT}{2v_f} f(\alpha - \beta) \right. \\ &\quad \quad \left. \Theta(x_i - x_\beta) e^{-i\Omega\tau_\beta - \Omega(x_\beta - x_i)/v} \frac{-iT}{2v_f} f(\beta - \alpha) \right] \left. \right\}. \quad (\text{A.4}) \end{aligned}$$

The  $(-1)$  in front is due to the sorting of the arguments of the sinh's to the correct pole structure  $(z - z_0)^{-1}$ , the  $2\pi i$  comes from the residue theorem, the factor  $-iT/2v_f$  is the prefactor of the sinh and  $(\pi T i)^{-1}$  is the strength of the pole. The negative sign in front of  $\Theta(\Omega)$  stems from the integration in the lower half plane. We also used a short handed notation

$$f(\alpha - \beta) = \sinh^{-1} \left[ \pi T \left( \frac{x_\alpha - x_\beta}{v_f} + i(\tau_\alpha - \tau_\beta) \right) \right]. \quad (\text{A.5})$$

Most parts of the prefactor cancels out, the only thing remaining is  $i/v_f$ . Furthermore we can identify

$$\frac{-iT}{2v_f} f(\alpha - \beta) = g_0^R(x_\alpha - x_\beta, \tau_\alpha - \tau_\beta). \quad (\text{A.6})$$

Using the  $\Theta$ -functions, we can insert some moduli and get

$$\begin{aligned}
\mathcal{W}_{i,j}^{in,R} &= \frac{-i}{v_f} e^{i(k_{f,i}x_\alpha - k_{f,j}x_\beta)} \times \\
&\times \int dx \left\{ e^{[-i(\Omega\tau_\alpha - \Delta kx) - |\Omega||x_\alpha - x|/v_f - \Gamma(|x_\alpha - x| + |x_\beta - x|)]} \times \right. \\
&\quad \times (\Theta(\Omega)\Theta(x_\alpha - x) - \Theta(-\Omega)\Theta(x - x_\alpha)) - \\
&\quad - e^{[-i(\Omega\tau_\beta - \Delta kx) - |\Omega||x_\beta - x|/v_f - \Gamma(|x_\alpha - x| + |x_\beta - x|)]} \times \\
&\quad \left. \times (\Theta(\Omega)\Theta(x_\beta - x) - \Theta(-\Omega)\Theta(x - x_\beta)) \right\} \\
&= \frac{-i}{v_f} e^{i(k_{f,i}x_\alpha - k_{f,j}x_\beta)} \int dx [\xi_\alpha - \xi_\beta], \tag{A.7}
\end{aligned}$$

where the function  $\xi_\alpha$  is given by

$$\begin{aligned}
\xi_\alpha &= e^{[-i(\Omega\tau_\alpha - \Delta kx) - |\Omega||x_\alpha - x|/v_f - \Gamma(|x_\alpha - x| + |x_\beta - x|)]} \times \\
&\quad \times \left\{ \Theta(\Omega)\Theta(x_\alpha - x) [\Theta(x_\beta - x) + \Theta(x - x_\beta)] \right. \\
&\quad \left. - \Theta(-\Omega)\Theta(x - x_\alpha) [\Theta(x_\beta - x) + \Theta(x - x_\beta)] \right\}, \tag{A.8}
\end{aligned}$$

with  $\Delta k = k_{f,j} - k_{f,i}$ .  $\xi_\beta$  is the same as  $\xi_\alpha$  but with  $\alpha \leftrightarrow \beta$ . Note that we inserted a factor of  $\Theta(x) + \Theta(-x) = 1$ . Using all the  $\Theta$  functions helps us evaluating the moduli. After the moduli have been evaluated, it is easy to compute the integrals. We still have to retain the  $\Theta$  functions, but in the end we get

$$\begin{aligned}
\int dx \xi_\alpha &= \frac{e^{\Gamma|x_\alpha - x_\beta|}}{|\Omega|/v_f + 2\Gamma + i\text{sgn}(\Omega)\Delta k} e^{-i\Omega\tau_\alpha} e^{i\Delta kx_\alpha} \left\{ \text{sgn}(\Omega) + \right. \\
&\quad + \frac{2\Gamma}{|\Omega|/v_f + i\text{sgn}(\Omega)\Delta k} (\Theta(\Omega)\Theta(x_\alpha - x_\beta) - \Theta(-\Omega)\Theta(x_\beta - x_\alpha)) \times \\
&\quad \left. \times \left( 1 - e^{-(|\Omega|/v_f + i\text{sgn}(\Omega)\Delta k)|x_\alpha - x_\beta|} \right) \right\}, \tag{A.9}
\end{aligned}$$

so eventually

$$\begin{aligned}
\int dx (\xi_\alpha - \xi_\beta) &= \frac{e^{\Gamma|x_\alpha - x_\beta|}}{|\Omega|/v_f + 2\Gamma + i\text{sgn}(\Omega)\Delta k} \left\{ \text{sgn}(\Omega) \left[ e^{-i\Omega\tau_\alpha} e^{i\Delta kx_\alpha} - e^{-i\Omega\tau_\beta} e^{i\Delta kx_\beta} \right] + \right. \\
&\quad + \frac{2\Gamma}{|\Omega|/v_f + i\text{sgn}(\Omega)\Delta k} \left( 1 - e^{-(|\Omega|/v_f + i\text{sgn}(\Omega)\Delta k)|x_\alpha - x_\beta|} \right) \times \\
&\quad \times \left[ (\Theta(\Omega)\Theta(x_\alpha - x_\beta) - \Theta(-\Omega)\Theta(x_\beta - x_\alpha)) e^{-i\Omega\tau_\alpha} e^{i\Delta kx_\alpha} - \right. \\
&\quad \left. - (\Theta(\Omega)\Theta(x_\beta - x_\alpha) - \Theta(-\Omega)\Theta(x_\alpha - x_\beta)) e^{-i\Omega\tau_\beta} e^{i\Delta kx_\beta} \right] \left. \right\}. \tag{A.10}
\end{aligned}$$

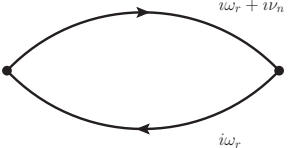
We are now quite finished with the calculation and the result has become quite big, so we try to simplify it. First of all we don't need the cutoff anymore since the integrand in (6.23) is decaying on a scale of  $l_{ee} \ll l$ . One can also see that the second term in the big

curly brackets is proportional to  $\Gamma = l^{-1}$  and can be omitted for  $l_\phi/l \ll 1$ . Performing these simplifications and inserting the result in equation (A.7) yields

$$\mathcal{W}_{i,j}^{in,R} = -i \frac{\text{sgn}(\Omega)}{|\Omega| + 2v_f/l + i\text{sgn}(\Omega)v_f\Delta k} \left( e^{-i\Omega\tau_\alpha} e^{-ik_{f,j}(x_\beta - x_\alpha)} - e^{-i\Omega\tau_\beta} e^{-ik_{f,i}(x_\beta - x_\alpha)} \right). \quad (\text{A.11})$$

## B. Matsubara sum for DC-current

This appendix is devoted to the calculation of the Matsubara sum in eq.(6.3). We know from chapter 2, that the conductivity is in principle given by closed fermionic loops (see e.g. fig. 2.1) times some prefactor. Since our goal is simply to perform the Matsubara sum, we forget about most of the prefactor and only consider the prefactor  $T/\nu_n$  in our calculation. When we forget about the momentum, the simplest bubble reads:



$$= -\frac{T}{\nu_n} \sum_{\omega_r} G(i\omega_r + i\nu_n)G(i\omega_r). \quad (\text{B.1})$$

We keep in mind that there is still a momentum integration to be done. Remembering the structure of the time-ordered Greens function

$$G(i\omega_r, k) = \frac{1}{i\omega_r - \epsilon(k) + i\text{sgn}(\omega_r)/2\tau}, \quad (\text{B.2})$$

one notices that the integral B.1 is only different from zero when the poles of the Greens functions lie on different half planes. This restricts our Matsubara sum to the region  $-\nu_n < \omega_r < 0$ .

We write now the sum over Matsubara frequencies as an integral

$$T \sum_{\omega_r} F(i\omega_r) = - \oint_C \frac{d\epsilon}{2\pi i} F(\epsilon) f(\epsilon) \quad (\text{B.3})$$

where  $f(\epsilon)$  is the Fermi distribution function and  $C$  is a contour enclosing all Matsubara frequencies. This method can be looked up in [8, 11], for instance.

We now extend the integration contour to  $\pm\infty$  as depicted in fig. B.1. The integration paths at  $\pm\infty$  vanish, so one is left with

$$\oint_C \frac{d\epsilon}{2\pi i} F(\epsilon) f(\epsilon) = \int_{-\infty}^{\infty} \frac{d\epsilon}{2\pi i} f(\epsilon - i\nu_n) F(\epsilon - i\nu_n) - \int_{-\infty}^{\infty} \frac{d\epsilon}{2\pi i} f(\epsilon) F(\epsilon). \quad (\text{B.4})$$

Interpreting  $G(i\omega_r + i\nu_n)G(i\omega_r) = F_{i\nu_n}(i\omega_r)$  we find

$$\begin{aligned} -\frac{T}{\nu_n} \sum_{\omega_r} G(i\omega_r + i\nu_n)G(i\omega_r) &= \\ &= \frac{1}{\nu_n} \frac{1}{2\pi i} \left[ \int_{-\infty}^{\infty} d\epsilon f(\epsilon - i\nu_n) F(\epsilon - i\nu_n) - \int_{-\infty}^{\infty} d\epsilon f(\epsilon) F(\epsilon) \right] \\ &= \frac{1}{i\nu_n} \frac{1}{2\pi} \left[ \int_{-\infty}^{\infty} d\epsilon f(\epsilon - i\nu_n) F(\epsilon - i\nu_n) - \int_{-\infty}^{\infty} d\epsilon f(\epsilon) F(\epsilon) \right] \\ &\rightarrow \frac{1}{\nu} \frac{1}{2\pi} \left[ \int_{-\infty}^{\infty} d\epsilon f(\epsilon - \nu) F(\epsilon - \nu) - \int_{-\infty}^{\infty} d\epsilon f(\epsilon) F(\epsilon) \right]. \end{aligned} \quad (\text{B.5})$$

In the last line we have performed the analytic continuation  $i\nu_n \rightarrow \nu + i0$ . Notice that our formula has the structure of a difference quotient, so taking the DC limit  $\nu \rightarrow 0$  leads us

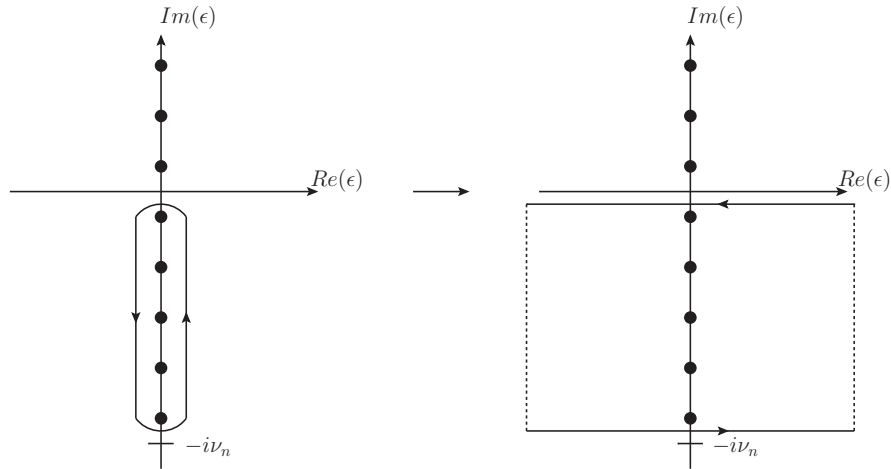


Figure B.1.: Deformation of the integration contour. Dots denote fermionic Matsubara frequencies.  $\nu_n$  is a bosonic matsubara frequency, so it lies between to fermionic ones.

to a derivative. Assuming  $F(\epsilon)$  is mostly flat, we can take it out of the derivative and one finally gets

$$-\frac{T}{\nu_n} \sum_{\omega_r} G(i\omega_r + i\nu_n)G(i\omega_r) = \int \frac{d\epsilon}{2\pi} F(\epsilon) \left( -\frac{df(\epsilon)}{d\epsilon} \right), \quad (\text{B.6})$$

where  $F(\epsilon)$  is given by

$$F(\epsilon) = G^R(\epsilon)G^A(\epsilon). \quad (\text{B.7})$$

$G^R$  is the retarded,  $G^A$  the advanced Greens function, this structure stems from our analytic continuation  $i\nu_n \rightarrow \nu + i0$ .

We can apply the same technique for bubbles containing disorder lines: Since scattering off disorder does not change frequency, the upper Greens functions still carry the frequency  $i\omega_r + i\nu_n$  and the lower ones  $i\omega_r$ . So including disorder scattering just affects the structure of the  $F(i\omega_r)$ -function, but the general technique can still be applied.

## C. Full Greens function in the Functional Bosonization approach

This Appendix is devoted to the Full Greens functions obtained by the Functional Bosonization approach presented in chapter 4. The whole derivation can be looked up in [19] and [37].

We start in space-time-representation. The Full Greens function is given by

$$G^R(x, \tau) = g_0^R(x, \tau) \exp[-B_{++}(x, \tau)], \quad (\text{C.1})$$

$g_0^{R/L}(x, \tau)$  is the free Greens function

$$g_0^R(x, \tau) = \mp \frac{iT}{2v_f} \frac{1}{\sinh[\pi T(x/v_f \pm i\tau)]} \quad (\text{C.2})$$

and the  $B_{\mu\nu}(x, \tau)$ -correlators are defined by

$$\begin{aligned} B_{R,R/L}(x, \tau) &= T \sum_n \int \frac{dq}{2\pi} (e^{iqx - i\Omega_n \tau} - 1) \frac{V(q, i\Omega_n)}{(v_f q - i\Omega_n)(\pm v_f q - i\Omega_n)}, \\ B_{LL}(x, \tau) &= B_{RR}(x, \tau), \\ B_{LR}(x, \tau) &= B_{RL}(x, \tau). \end{aligned} \quad (\text{C.3})$$

$V(q, i\Omega_n)$  is the dynamically screened interaction. Introducing a dimensionless coupling constant  $y \simeq g/2\pi v_f$  and a renormalized Fermi velocity  $u = v_f \sqrt{1 + 4y}$  one finds for the spinless case

$$B_{RR}(x, \tau) = -\ln \eta(x, \tau) - \frac{\tilde{y}}{2} \ln \varsigma(x, \tau), \quad B_{RL}(x, \tau) = -\frac{\tilde{y}_r}{2} \ln \varsigma(x, \tau) \quad (\text{C.4})$$

and for the spinful case

$$B_{RR}(x, \tau) = -\frac{1}{2} \ln \eta(x, \tau) - \frac{\tilde{y}}{4} \ln \varsigma(x, \tau), \quad B_{RL}(x, \tau) = -\frac{\tilde{y}_r}{4} \ln \varsigma(x, \tau). \quad (\text{C.5})$$

The functions  $\varsigma$  and  $\eta$  are given by

$$\begin{aligned} \varsigma(x, \tau) &= \frac{(\pi T/\Lambda)^2}{\sinh[\pi T(x/u + i\tau)] \sinh[\pi T(x/u - i\tau)]}, \\ \eta(x, \tau) &= \frac{v_f \sinh[\pi T(x/v_f + i\tau)]}{u \sinh[\pi T(x/u + i\tau)]}, \end{aligned} \quad (\text{C.6})$$

where  $\Lambda$  is some high-energy cutoff and the prefactors are given by

$$\tilde{y} = \frac{(u - v_f)^2}{2uv_f}, \quad \tilde{y}_r = \frac{u^2 - v_f^2}{2uv_f}. \quad (\text{C.7})$$

Using these functions one finds for the spinless Greens function

$$G^R(x, \tau) = -\frac{i}{2\pi u} \frac{\pi T}{\sinh[\pi T(x/u + i\tau)]} \left\{ \frac{\pi T/\Lambda}{\sinh[\pi T(x/u + i\tau)]} \frac{\pi T/\Lambda}{\sinh[\pi T(x/u - i\tau)]} \right\}^{\tilde{y}/2} \quad (\text{C.8})$$

and for the spinful one

$$G^R(x, \tau) = -\frac{i}{2\pi\sqrt{uv_f}} \left\{ \frac{\pi T}{\sinh[\pi T(x/v_f + i\tau)]} \frac{\pi T}{\sinh[\pi T(x/u + i\tau)]} \right\}^{1/2} \times \left\{ \frac{\pi T/\Lambda}{\sinh[\pi T(x/u + i\tau)]} \frac{\pi T/\Lambda}{\sinh[\pi T(x/u - i\tau)]} \right\}^{\tilde{y}/4}. \quad (\text{C.9})$$

Since we only the spinful Greens functions need in our calculation, we perform the next steps only for these and leave the spinless ones as they are. In section 6.2 we need the space-energy-representation of the Greens functions, so we Fourier transform eq. (C.9) with respect to  $\tau$  and get

$$\int_0^{1/T} d\tau \exp i\epsilon_n \tau G^R(x, \tau) = G_r^R(x, i\epsilon_n) - G_a^R(x, i\epsilon_n) \quad (\text{C.10})$$

where  $\epsilon_n$  are fermionic Matsubara frequencies and

$$G_r^R(x, i\epsilon_n) = \Theta(\epsilon_n)\Theta(x)\mathcal{G}(x, \epsilon_n), \quad G_a^R(x, i\epsilon_n) = \Theta(-\epsilon_n)\Theta(-x)\mathcal{G}(x, \epsilon_n), \quad (\text{C.11a})$$

$$\mathcal{G}(x, \epsilon_n) = \frac{\exp(-|\epsilon_n x|/u + |x|/2l_{ee})}{i\sqrt{uv}} {}_2F_1[1/2 + \xi_n, 1/2, 1; \chi(|x|)], \quad (\text{C.11b})$$

$$\chi(x) = 1 - \exp(2x/l_{ee}), \quad \xi_n = \epsilon_n/2\pi T. \quad (\text{C.11c})$$

${}_2F_1(a, b, c; z)$  is the hypergeometric function and for left movers  $G_{r,a}^R(x, i\epsilon_n) = G_{r,a}^L(-x, i\epsilon_n)$  holds. Note that the indices  $a$  and  $r$  do *not* denote retarded and advanced Greens functions, these are just indices denoting the behaviour of the  $\Theta$ -functions.

We also show the momentum-energy Greens functions for completeness, although we don't need these in our calculation. Fourier transforming the space-energy Greens functions and analytically continuing the result yields

$$G_{R/A}^R(q, \epsilon) = \frac{2l_{ee}}{\sqrt{uv_f}} \mathcal{P}(\pm\kappa_u) \mathcal{P}(\pm\kappa_{v_f}) \quad (\text{C.12})$$

with

$$\kappa_u = (\epsilon/u - q)l_{ee}, \quad \kappa_{v_f} = (\epsilon/v_f - q)l_{ee} \quad (\text{C.13})$$

and

$$\mathcal{P}(z) = \frac{\Gamma[(1 - 2iz)/4]}{\Gamma[(3 - 2iz)/4]}. \quad (\text{C.14})$$

The electron-electron scattering length is defined by

$$l_{ee} = \frac{u_-}{2\pi T} \quad (\text{C.15})$$

with

$$\frac{1}{u_-} = \frac{1}{2} \left( \frac{1}{v_f} - \frac{1}{u} \right). \quad (\text{C.16})$$